A Smart and Versatile Theranostic Nanomedicine Platform based on Nanoporphyrin

Yuanpei Li[#1,*], **Tzu-yin Lin**[#2], **Yan Luo**[1,8], **Qiangqiang Liu**[1,9], **Wenwu Xiao**[1], **Wenchang Guo**[1], **Diana Lac**[1], **Hongyong Zhang**[2], **Caihong Feng**[1,10], **Sebastian Wachsmann-Hogiu**[3,6], **Jeffrey H. Walton**[1,4], **Simon R. Cherry**[5], **Douglas J. Rowland**[5], **David Kukis**[5], **Chongxian Pan**[2,7,*], and **Kit S. Lam**[1,*]

[1] Department of Biochemistry and Molecular Medicine, UC Davis Comprehensive Cancer Center, University of California Davis, Sacramento, CA 95817, USA

[2] Department of Internal Medicine, Division of Hematology/Oncology, University of California Davis, Sacramento, CA 95817, USA

[3] NSF Center for Biophotonics Science and Technology, University of California Davis, Sacramento, CA 95817, USA

[4] UC Davis NMR Facility, Davis, CA 95616, USA

[5] Department of Biomedical Engineering, Center for Molecular and Genomic Imaging, University of California Davis, Davis, CA 95616, USA

[6] Department of Pathology and Laboratory Medicine, University of California Davis, Sacramento, CA 95817, USA

[7] VA Northern California Health Care System, Mather, CA.

[8] Department of Oncology, PLA Cancer Research Institute of the Second Affiliated Hospital, Third Military Medical University, Chongqing, 400037, China

[9] National Chengdu Center for Safety Evaluation of Drugs, West China Hospital, Sichuan University, Chengdu, 610041, China

[10] Beijing institute of technology, Beijing, 100081, China.

[#] These authors contributed equally to this work.

*Correspondence should be addressed to K.S.L.(kit.lam@ucdmc.ucdavis.edu), C.P.(cxpan@ucdavis.edu) or Y.L. (lypli@ucdavis.edu).

Abstract

Multifunctional nanoparticles with combined diagnostic and therapeutic functions show great promise towards personalized nanomedicine. However, attaining consistently high performance of these functions *in vivo* in one single nano-construct remains extremely challenging. Here we demonstrate the use of one single polymer to develop a smart "all-in-one" nanoporphyrin platform that conveniently integrates a broad range of clinically relevant functions. Nanoporphyrins can be used as amplifiable multimodality nanoprobes for near-infrared fluorescence imaging (NIRFI), magnetic resonance imaging (MRI), positron emission tomography (PET) and dual modal PET-MRI. Nanoporphyrins greatly increase the imaging sensitivity for tumor detection through background suppression in blood, as well as preferential accumulation and signal amplification in tumors. Nanoporphyrins also function as multiphase nanotransducers that can efficiently convert light to heat inside tumors for photothermal-therapy (PTT), and light to singlet oxygen for photodynamic-therapy (PDT). Furthermore, nanoporphyrins act as programmable releasing nanocarriers for targeted delivery of drugs into tumors.

INTRODUCTION

Nanoparticle-based theranostic agents are emerging as a promising paradigm towards personalized nanomedicine for disease- and patient-specific diagnosis and treatment [1-4]. The integration of imaging and therapeutic functions into a single nano-formulation allows precise diagnosis of disease, individualized selection of treatment modality, real-time monitoring of drug distribution/delivery and assessment of therapeutic outcomes[5-7]. Although conceptually impressive, these theranostic agents are still at an early stage of development. A variety of inorganic and organic-based nanoparticles have been proposed but each type of nanoparticle displays distinct advantages and limitations. Inorganic nanoparticles often have unique physicochemical properties that allow applications in imaging and even therapy. For example, semiconductor quantum dots (QDs)[8], super paramagnetic iron oxide nanoparticles (SPIO-nanoparticles) [9,10], or gold-based nanomaterials[11,12] are valuable fluorescence probes, MRI contrast agents and photo-absorbers for photothermal therapy[11,12], respectively. Although promising, these inorganic nanoparticles have not yet achieved broad clinical application due to concerns about their long-term safety and surface-dependent drug loading property[7,13]. On the contrary, several "soft" organic nanoparticles (e.g. paclitaxel-loaded polymeric micelles (Genexol-PM®), liposomal doxorubicin (Doxil®) and paclitaxel-loaded human serum albumin nanoaggregate (Abraxane®)) have been approved or are currently in clinical trials for the treatment of human cancers because of their excellent biocompatibility and drug loading capacity. However, these organic nanoparticles have been used mainly as drug carriers since they generally lack imaging functions and intrinsic light absorbing ability for phototherapy. Additional efforts are usually needed to attach or encapsulate both therapeutic molecules and imaging agents[4]. Notably, a few organic nanoparticles, such as porphysome nanovesicles generated by porphyrin/lipid bilayers[7] and conductive polymer nanoparticles[14], have recently been proposed as agents to transduce light to heat for photothermal therapy (PTT) against cancers. However, these nanoparticles tend to have high liver and spleen accumulation, in part due to their relatively large size (~100 nm), resulting in non-specific

clearance by the reticuloendothelial system, obviating the advantage of preferential tumor targeting over normal organs via enhanced permeability retention (EPR) effect [15-17].

Furthermore, the theranostic nanoparticles reported thus far are only able to integrate limited number of clinically useful functions, thus narrowing their usefulness for diagnosis and treatment. Concerns also remain with many multifunctional nanoparticles regarding complexity of fabrication, unfavourable biodistribution and limited ability to regulate release of payload. In addition, high background noise and lack of an amplification strategy to increase the target's signal output are major factors hampering advances in nanoparticle imaging functions [18]. There is a need for the development of biocompatible nanoplatforms that integrate a variety of recently advanced and clinically relevant imaging and therapeutic modalities. To successfully achieve multifunctionality, nanoparticles should be straightforward to prepare and "intelligent" enough to overcome *in vivo* biological barriers such as interactions with blood proteins[19], lipoproteins, blood cells, blood vessel walls, and the reticuloendothelial system, and be able to deliver drugs and imaging agents efficiently in a targeted manner to diseased tissues.

Here we report on a robust, smart and highly versatile "all-in-one" porphyrin-based organic nanoconstruct (named nanoporphyrin, or NP) that can be constructed by using a single organic building block, a porphyrin/cholic acid hybrid polymer (Fig. 1a,b). This NP platform integrates a variety of imaging and therapeutic functions that include imaging (near infra-red fluorescent imaging (NIRFI), positron emission tomography (PET), magnetic resonance tomography (MRI), dual modal PET-MRI), photothermal therapy (PTT), photodynamic therapy (PDT), as well as targeted drug delivery (Fig. 1a,b).

RESULTS

Synthesis and characterization of NPs

NPs were formed by the self-assembly of a novel class of hybrid amphiphilic polymers (called telodendrimers) comprised of linear polyethylene glycol (PEG) and dendritic oligomers of pyropheophorbide-a (Por, a porphyrin analogue) and cholic acid (CA) (Fig. 1a, Supplementary Fig. 1-3). PEG^{5k}-Por_4-CA_4, a representative telodendrimer, is shown in Fig 1a and Supplementary Fig. 1. Dynamic light scattering (DLS) showed the particle size of NPs to be about 21 ± 6 nm (Supplementary Fig. 4). Based on the molecular weight of telodendrimer and the total molecular weight of nanoparticle measured on DLS, we estimated that one NP nanoparticle was formed by the assembly of ~100 telodendrimers. Independently, transmission electron microscopy (TEM) showed that the NPs were spherical with a size of 21 nm (Fig. 1c) agreeing with DLS measurements. NPs have two absorption peaks, one at 405 nm and one in the near-infrared (NIR) range with peak at ~680 nm (Fig. 1d). PEG^{5k}-Por_4-CA_4 has the intrinsic ability to chelate a variety of metal ions, such as copper (Cu(II)), palladium (Pd(II)), gadolinium (Gd(III)) and gallium (Ga(III)). Metal ion-loaded NPs, generated by the self-assembly of these metal complexed-telodendrimers in PBS, were found to exhibit a unique absorbance peaks ranging between 650-690 nm (Fig. 1d). When metal ions are loaded into the porphyrin components of the NPs, the heavy atoms show a higher scattering power, leading to more phase shift and higher contrast in TEM.

Thus the metal ion layer within the NP can be observed under TEM even without staining (Supplementary Fig. 5).

When excited at 405 nm, the NPs formulated in phosphate buffered saline (PBS) showed a very weak red fluorescence emission with a peak value at 680 nm (Fig. 1e, red curve). This is not unexpected because of the π-π interactions and hydrophobic characteristics of Por molecules, which can easily form highly ordered structures in the interphase between the PEG corona and the hydrophobic core of the micellar NPs, contributing to the strong self-quenching effect of the excited state in the aqueous medium[20]. In contrast, when the NPs were disrupted by sodium dodecyl sulfate (SDS)[21,22] (Supplementary Fig. 4), strong fluorescence at 680 nm was observed when excited at 405 nm (Fig. 1e, blue curve). Fig. 1f compares the NIR fluorescence of NPs as a function of NP concentration, with or without addition of SDS (Supplementary Fig. 6). It is clear that NIR fluorescent signal of the NPs is greatly amplified upon micellar dissociation, which is expected to occur at tumor sites and/or inside the tumor cells. We have used our previously reported PEG^{5k}-CA_8 micelles[16,21,23-25] as a conventional micelle-based nanocarrier to physically encapsulate Por for comparison. NPs demonstrated 10 times more self-quenching than PEG^{5k}-CA_8 micelles (NM-POR) encapsulating the same concentration of Por (Supplementary Fig. 7,8), indicating quenching was a distinct characteristic of Por molecules that were assembled in the core of a nanoporphyrin construct. Similar to the fluorescence property, NPs also possess architecture-dependent "on/off" photodynamic transduction. Generation of reactive oxygen species (ROS) by NPs in PBS after light irradiation was minimal, but could be restored upon the addition of SDS, measured by using singlet oxygen sensor green (SOSG) as a highly selective singlet oxygen indicator (Fig. 1g) [26,27].

As NPs are highly self-quenched in PBS, energy is released in the form of heat instead of fluorescence and/or singlet-oxygen generation upon laser irradiation (Fig. 1h,i). The temperature of the NP solution increased from 24 °C to 62 °C as NP concentrations increased from 0 to 1.0 mg/mL. When NPs were dissociated in the presence of SDS and illuminated with the same dose of light, strong fluorescence but less significant increase in solution temperature was observed (Fig. 1h,i). To the contrary, NM-POR only showed moderate temperature increase in PBS compared to that in SDS with the same level of illumination (Supplementary Fig. 9), indicating the photothermal transduction was efficient only when Por was confined to the interphase between the PEG corona and the hydrophobic core of the micellar NPs.

Blood is the first biological barrier for nanoparticle-based drug delivery systems via intravenous administration. Interaction with blood proteins and lipoproteins may cause the dissociation of nanoparticles and lead to premature drug release[19]. In order to further increase the structural stability of NPs in blood circulation, we have applied reversible disulfide crosslinking strategy[19,21] to the NP platform. Four cysteines were introduced to the oligolysine backbone of the telodendrimer to form PEG^{5k}-Cys_4-Por_4-CA_4 (Fig. 2a, Supplementary Fig. 10, 11). The resulting NPs were then crosslinked via disulfide bond through oxidation of the thiol groups on the cysteines[21,28]. TEM showed that these disulfide crosslinked NPs (CNPs) were spherical vesicles of 32±8 nm in diameter (Fig 2b). Such CNPs retained their particle size even in the presence of SDS but were dissociated with the

addition of both SDS and reducing agents (Supplementary Fig. 12). Similar to the NPs, the fluorescence of CNPs was also highly quenched in PBS. Correspondingly, the fluorescence of CNPs was restored in the presence of both SDS and endogenous reducing agent such as glutathione (GSH) at intra-cellular levels[21] (Fig. 2c).

We have previously reported a series of cholic acid-based telodendrimer nano-carriers for efficient encapsulation and delivery of anti-cancer drugs, such as paclitaxel (PTX)[21,23], vincristine (VCR)[25], and doxorubicin (DOX)[29]. We found that CNPs could also efficiently carry a variety of poorly water-soluble chemotherapeutic drugs and molecularly targeted drugs. For instance, DOX could be efficiently encapsulated inside CNPs with a loading capacity of 2.90 mg/mL (Fig. 2d). When formulated at 2.55 mg/mL, the drug loading efficiency of DOX-loaded CNPs (CNP-DOX) was above 85% with final particle size around 30 nm (Fig. 2d). We then investigated the interaction of CNP-DOX with human plasma to simulate the destabilizing conditions in blood for *in vivo* applications and found that the particle size of CNP-DOX was highly stable (Supplementary Fig. 13). We utilized the fluorescence resonance energy transfer (FRET) between the doxorubicin and NPs to monitor the real time drug release in human plasma (Fig. 2e). As shown in Fig. 2f,g, the FRET signal was very stable when CNP-DOX was incubated in human plasma for 24 hrs at 37 °C, indicating the doxorubicin release from CNPs was slow. However, there was dramatic and immediate FRET signal decrease with each light exposure at 24 hrs and 28 hrs (Fig. 2f,g), indicating that CNPs could be triggered to release drug via illumination, probably as a result of local heat generation. As expected, DOX release could also be triggered by GSH at intra-cellular level (~10 mM)[21], as monitored by FRET (Fig 2h). We have also determined the release profiles of DOX from CNPs under similar conditions by dialysis method[21]. Those results indicated that DOX release was slow in the presence of human plasma but could be facilitated through illumination or by adding GSH (~10 mM) (Fig 2i). The DOX release profiles measured by dialysis method were consistent with that determined by FRET approach.

Validation of NPs in cancer cell lines

Intracellular delivery of CNP-DOX was investigated in SKOV3 ovarian cancer cells (Fig 3a). After 2 hrs of incubation, DOX was released from CNPs and transported into nucleus, while the NIR fluorescence from disassociated CNPs (unquenched telodendrimers) remained in the cytoplasm. To further study the relationship between the dissociation property of CNPs and intracellular GSH level, we conducted the cell uptake experiments on three cell lines: SKOV3 ovarian cancer cell line, PC3m prostate cancer cell line and MB49 mouse bladder cancer cell line. The order of GSH level of these cell lines is PC3m>SKOV3>MB49, as measured by an indicator, ThiolTracker™ Violet (Supplementary Fig. 14). We found that in these cells intracellular GSH levels correlated positively with intracellular dissociation of CNPs, indicating that the disulfide crosslinks in CNPs are reversible.

Without light irradiation, the intact CNPs showed no observable cytotoxicity up to 1.0 mg/mL against SKOV3 ovarian cancer cells while free Por showed significant dark phototoxicity in a dose-dependent manner (Supplementary Fig. 15). The efficacy of CNP-

mediated PDT *in vitro* was found to be light-dose and CNP-dose dependent (Fig. 3b,c). CNPs were much more cytotoxic than 5-aminolevulinic acid (5-ALA, a FDA approved agent for PDT) using the same illumination dose (Fig. 3c). The loss of cell viability was found to be associated with intracellular ROS production (Fig. 3d), resulting in loss of mitochondrial membrane potential, cellular damage, and cell apoptosis as evidenced by caspase3/7 activation (Fig. 3e-g). Moreover, we found that CNP-DOX mediated combination chemotherapy and photo-therapy was significantly more efficacious than CNP mediated photo-therapy alone, free DOX, or NM-DOX (DOX loaded standard cholic acid-telodendrimer-based micelles[21] without porphyrin) after illumination at corresponding doses of light (Fig. 3h).

NP mediated multimodal imaging in animal models

In order to exploit nanoporphyrins as nanoprobes for *in vivo* imaging, it is important to first investigate their pharmacokinetics and biodistribution. *In vivo* blood elimination kinetic studies indicated CNPs possess a longer circulation time in comparison with non-crosslinked NPs, indicating the enhanced *in vivo* stability of NPs with crosslinking (Fig 4a). In order to quantitatively determine the distribution of nanoporphyrins in tissues, Gd(III) chelated non-crosslinked nanoporphyrins (Gd-NPs) and Gd(III) chelated CNPs (Gd-CNPs) were prepared and injected intravenously into nude mice bearing SKOV3 ovarian cancer xenograft. Twenty four hours post-injection, Gd concentration in tumor and normal organs was measured by inductively coupled plasma mass spectrometry (ICP-MS). As shown in Fig 4b, significant accumulation of Gd in the SKOV3 tumors was noted 24 hrs after Gd-NPs and Gd-CNPs administration in comparison with clinical formulation of gadolinium diethylenetriaminepentacetate complex (Gd-DTPA) designed for MRI imaging. Gd-CNPs accumulated 2.8 and 12.3 times more in tumor than Gd-NPs and Gd-DTPA, respectively. In addition, administration of Gd-CNPs resulted in significantly lower Gd uptake by liver and spleen when compared to Gd-NPs and Gd-DTPA. Furthermore, it should be noted that in the Gd-CNPs group, Gd uptake by a tumor was much higher than that by liver and spleen.

The particle sizes of CNPs were around 32 nm (Fig. 2b), which is an optimal range for tumor targeting and penetration[15,16]. On the basis of their relatively small size, reversibly crosslinking nature and unique architecture-dependent fluorescence property, CNPs are particularly suitable to be used as activatable optical nanoprobes to increase the sensitivity of NIRFI for improved cancer detection through background suppression in blood, as well as preferential accumulation and signal amplification at tumor site. The CNPs could stay silent (or in the OFF state) with minimum background fluorescence signals in blood circulation (Fig. 5a, lower panel). The quenching status of CNPs in blood was further demonstrated by the recovery of fluorescence via the addition of SDS and GSH (Supplementary Fig. 16). As expected, the overall fluorescence signal in the whole body was drastically lower for CNPs than non-crosslinked NPs after intravenous injection in nude mice bearing SKOV3 ovarian cancer xenograft (Fig. 5a). Upon accumulation at the tumor site *via* the size-mediated EPR effect, these crosslinked nanoprobes could be turned ON via the cleavage of disulfide bonds by the endogenous reducing agent GSH at tumor site or in cancer cells[21], followed by micellar dissociation and amplification of fluorescence signal (Fig 3a, Supplementary Fig. 14). CNPs showed significantly higher tumor accumulation

than non-crosslinked NPs at 24 hrs post-injection (Fig. 5a), in agreement with the biodistribution of Gd-loaded nanoporphyrins (Fig 4b). *Ex vivo* NIRF imaging at 24 hrs post-injection showed both non-crosslinked NPs and CNPs had superior fluorescence signal in tumors compared to normal organs (Fig. 5b). The average fluorescence signal of CNPs at tumor site was 15.2 times higher than that in muscle of the same group of mice and 3.1 times higher than that of non-crosslinked NPs at tumor site (Fig. 5c). The differential fluorescence signal between the CNPs and noncrosslinked NPs can be explained by the stability of the former construct in the circulation and higher uptake into the tumor (Fig 4a,b).

Fig. 5d shows projection images of the intra-tumoral distribution of the CNPs (red) obtained by Large-Scale-Imaging (LSI) laser scanning confocal microscope. The tumor blood vessels were labelled with Dextran-FITC (green). The overall NIRF signal from CNPs was very low inside the tumor tissue at 1 hr post-injection (Fig. 5d, left, Supplementary Movie 1). Significant NIRF signal was observed surrounding the blood vessels (green) at 24 hrs (Fig. 5d, middle, Supplementary Movie 2), indicating the accumulation and partial dissociation of CNPs into tumor tissue around blood vessels. At 48 hrs, NIRF signals diffused throughout the entire tumor implying excellent tissue penetration and dissociation of CNPs at the tumor site (Fig. 5d, right, Supplementary Movie 3). We further investigated the subcellular distributions of nanoporphyrins in tumor tissue. The NIRF signal inside tumor cells was low at 24 hrs post-injection of CNPs and increased significantly at 48 hrs post-injection (Supplementary Fig. 17). The fluorescence was mainly localized in the cytoplasm of cancer cells in a wispy to focal pattern at 48 hrs post-injection of CNPs. These results demonstrated the excellent delivery of nanoporphyrins to target tumor cells after intravenous injection.

We then investigated the NIRF imaging capability of CNPs in transgenic mice (10-12 weeks) with naturally occurring breast cancers (FVB/n Tg(MMTV-PyVmT)) through intravenous injection. After 24 hrs, high fluorescence was observed in all the spontaneous breast cancers (Fig. 5e), as CNPs accumulated in the tumors and inside the tumor cells, they dissociated and became unquenched. *Ex vivo* imaging further confirmed the preferential uptake of the CNPs in all nine excised breast tumors compared to normal organs after 24 hrs. In some experiments, we used older transgenic mice (20-24 weeks) and detected accumulation of NPs in metastatic lesions in the lungs with LSI laser scanning confocal microscope, including tiny lesions that measured less than 100 micron in diameter (Fig. 5f, Supplementary Fig. 18).

The nanoporphyrins have intrinsic ability to chelate Gd(III) (Fig. 1d), preferentially accumulate at the tumor sites and possess architecture-dependent magnetic resonance properties which permit their use as activatable contrast agents for sensitive and tumor-specific MRI. Similar to the fluorescence measurements in Fig. 1e,f, there is low MRI signal enhancement when Gd-NPs retain their micellar integrity in PBS (Fig. 6a). This is likely due to the stacking of Gd/Por at the interface between the hydrophobic core and hydrophilic corona, thus shielding Gd(III) from interacting with protons in water. Upon dissociation in SDS, the Gd ion chelated by the Por has access to nearby protons and therefore shorten their spin-lattice relaxation time, resulting in an enhancement of the MRI signal (Fig. 6a). This unique architectural feature of Gd-NPs offers the opportunity for sensitive MRI detection of

tumor as the background signal of the circulating NPs is low. We validated the application of Gd-NPs for MRI in transgenic mice with "spontaneous" mammary cancers. A set of representative slices at different time point post-injection is shown in Fig. 6b. We demonstrated that Gd-NPs could significantly enhance the contrast of tumor at 1.5 hrs post-injection with very low signal enhancement in normal tissue. The tumor contrast was sustained for more than 26 hrs. Doses of Gd used in these studies were equivalent to 1/7th of the clinically recommended Gd dose for human[30]. These results confirm that the MRI signal enhancement in the whole body is low when the Gd-NPs are circulating in blood. After reaching the tumor site or tumor cells, the Gd-NPs dissociate and allow the interaction of Gd ions with surrounding protons, resulting in the significant MRI contrast only at tumor site (Fig. 1b). The above data demonstrated Gd-NPs even without crosslinking have excellent performance as contrast agents for tumor-specific MRI. Gd-CNPs are expected to have even better properties for MRI than Gd-NPs due to superior tumor accumulation (Fig 4b). The investigation of Gd-CNPs as MRI contrast agents in animal models is on-going in our laboratory.

Furthermore, NPs have intrinsic capacity to incorporate radiotracers for applications as PET nanoprobes. For instance, we have incorporated of a radiotracer (^{64}Cu(II)) into NPs for PET imaging through a simple, fast, one-pot, high yielding radiolabeling strategy (radiochemical yields (RYC)>96.5%) (Fig. 1d, Supplementary Fig. 19). PET imaging showed that ^{64}Cu-NPs started to accumulate at tumor sites 4 hrs after injection, and reached maximum level at 16 hrs. After 24 hrs, the radiolabel was found primarily at the implanted tumors, with very low background signalling in the rest of the body (Fig. 6c).

The synergistic combination of PET and MRI is likely to become the next generation of dual-modality scanners to provide accurate diagnoses[31,32]. Consequently, there is a great need to develop dual-modality agents that can take advantage of the complementary strengths of PET (high sensitivity and quantifiability) and MR (high soft-tissue resolution) imaging[33-35]. As an exogenous-chelator-free nanoplatform that possesses intrinsic capacity to chelate Gd(III) and radiotracers simultaneously, NPs show significant promise for development as dual-modality nanoprobes for PET-MRI. We have shown both ^{64}Cu(II) and Gd(III) could be efficiently incorporated into NPs (Fig. 1d, Supplementary Fig. 19). Dual-labeled NPs could significantly enhance the MRI contrast and PET signal at the tumor site at 24 hrs post-injection (Fig. 6d,e). Interestingly, the heterogeneity of the tumor and the inhomogeneous distribution of NPs in the tumor were non-invasively revealed by PET-MRI (Fig. 6e).

NPs mediated multimodal therapy in animal models

Light-based therapies such as PDT and PTT may offer promising opportunities for cancer treatment[11,12,36-42]. There have been studies showing that PTT have synergistic effect with PDT [49,53,54]. Several inorganic nanoparticle complexes, such as photosensitizer conjugated gold nanorod[40], graphene oxide nanoparticles[43] and silica-coated palladium/silver nanoparticles[44], have been developed for PTT/PDT dual therapy. However, the activation of these nanoparticles required two separate illuminations with multiple-wavelength lasers (e.g. 808 nm and 675 nm) [40,43,44]. There are also concerns regarding the long-term safety of these

inorganic nanoparticles. Here we demonstrated the biocompatible nanoporphyrins could be used as a dual-modal nanotransducer that could be activated to release heat and ROS efficiently at tumor site for simultaneous PTT/PDT using a portable, single wavelength NIR laser.

The fluorescence of CNPs stayed quenched in blood after intravenous injection into mice bearing implanted tumor xenograft (Supplementary Fig. 20). Similarly, the ROS production of CNPs in blood was also minimal upon exposure with low dose light (similar to the sun light at 690 nm received in daily life, 0.1 W/cm^2) (Fig 7a). No obvious hemolysis was observed for CNPs in blood after light exposure (Supplementary Fig. 21). The heat generation of CNPs was also negligible after exposure to the same dose of light (Fig 7b, c). To the contrary, NM-POR, the Por encapsulated conventional micelles, presented 5 times higher fluorescence in blood of the mice than CNPs and produced significantly higher amount of ROS resulting in severe hemolysis (Fig 7a, Supplementary Fig. 20, 21). This is likely due to the less quenching effect of Por molecules when physically encapsulated inside micelles (Supplementary Fig. 9).

The tumors were illuminated with therapeutic dose of light (1.25 W/cm^2 for 120 s) 24 hrs after intravenous administration of PBS, CNPs and NM-POR. CNPs were found to elicit 2.5 times temperature increase and generate significantly higher amount of ROS at tumor site compared to NM-POR (Fig 7d,e Supplementary Fig. 22). Dramatically higher ROS production for CNP-treated group than PBS control group at the illuminated tumor site was further confirmed by using SOSG as an indicator (Supplementary Fig. 23). The simultaneous heat and ROS generation at tumor site in the CNP-treated group could be attributed to the significant accumulation of CNPs at tumor sites and partial dissociation 24 hrs after injection (Fig. 5d). Upon light irradiation, the intact CNPs are expected to generate heat while the dissociated CNPs could be activated to produce ROS. The above results suggested architecture dependent photonic properties of CNPs could be utilized to minimize the unintended toxicity of photosensitizers in blood and to deliver significantly higher amount of heat and ROS to tumor than comparable nanocarriers.

We have also demonstrated that the temperature at the tumor site of transgenic mice increased to 57 °C after light irradiation (1.25 W cm^{-2} for 2 min) 24 hrs after injection of CNPs (Fig. 8a,c). This temperature is sufficient to cause irreversible damage to cancer cells[7]. In contrast, the temperature at the tumor site in the PBS control group only increased to 41 °C with identical level of light exposure (Fig. 8b,c). The ROS generated by CNPs after irradiation was also significantly higher than the tissue background in the PBS control group, as measured by using DCF-DA (Fig. 8d) or SOSG (Supplementary Fig. 24) as indicators. Histopathology revealed large areas of severe tissue damage, such as cellular destruction and apoptosis at 24 hrs after irradiation (Fig. 8e) as evidenced by positive TUNEL results and cleaved caspase3 immuno-reactivity (Supplementary Fig. 25). These changes could be attributed to anti-tumor effects from both heat and ROS production (Fig. 8a,c,d).

We have shown in Fig. 2 that CNPs could be used as programmable releasing nanocarriers that minimized the drug release in human plasma but could be triggered to release the drug

content when exposed to light and intracellular reducing agents. Upon irradiation with near-infrared light, drug loaded CNPs are expected be activated to release singlet oxygen, heat and drugs simultaneously at the tumor sites for simultaneous PTT/PDT and chemotherapy. We have performed *in vivo* therapeutic studies to evaluate the anticancer efficacy of CNPs in transgenic and xenograft mouse models. In the transgenic mammary tumor mouse study, CNP-mediated PTT/PDT could significantly inhibit tumor growth with a light dose of 1.25 W cm^{-2} for 2 min once per week when compared to the PBS control group and NM-DOX group. The treated tumors were completely eliminated on day 12 with ulceration (Fig. 8f). No palpable tumors were detected even on day 32 (Fig. 8g). CNP-DOX mediated combination therapy of PTT/PDT with DOX showed similar efficacy (Fig. 8f,g). In order to effectively compare the efficacy of NP mediated combination therapy, we will need to use lower dose of NPs and/or lower dose of light. This will be the subject of future work. As expected, in nude mice bearing SKOV3 ovarian cancer xenograft, the NP mediated photo-therapy, free DOX and NMDOX treated groups all resulted in slower SKOV3 tumor growth than the PBS control group (Fig. 8h). At the same dose of DOX, photosensitizer (porphyrins) and light (0.25 W cm^{-2} for 2 min), the combination treatment with CNP-DOX showed the best antitumor activity and totally inhibited tumor growth throughout the study (Fig. 8h). No significant changes were observed in body weight, complete blood count, and serum chemistry after 3 doses of treatment (Supplementary Fig. 26, Table 1). Mice were handled without shielding ambient light in the laboratory, but no skin photo-toxicity was found.

MRI guided photo-therapy

Because NPs have intrinsic ability to chelate Gd(III), we can conveniently employ MRI to simultaneously monitor in real time the biodistribution of these nanoparticles and the tumor response. As a proof of concept, we used MRI to observe the tumor growth in SKOV3 ovarian cancer mice models after administration of Gd-NPs with or without illumination (Fig. 8i). MR images showed that Gd-NPs had significant accumulation at tumor site beginning 4 hrs post-injection. For the treatment group, tumors were illuminated at 24 hrs post-injection. MR images at 48 hrs post-injection (24 hrs after irradiation) showed both shrinkage of the tumor and increase in necrotic volume at the tumor site. MRI showed complete tumor elimination at 7 days post-injection. In contrast, MR imaging showed no difference in tumor size in control mice that were not illuminated.

DISCUSSION

The nanoporphyrin platform reported here possesses several properties that are unique and favourable as theranostic agents: 1) intrinsic ability to chelate imaging agents such as ^{64}Cu(II) and Gd(III), 2) excellent efficiency for drug loading, 3) unique architecture-dependent fluorescent, photothermal, photodynamic and magnetic resonance properties, 4) biocompatible, monodisperse, and relatively small (20~30 nm), and 5) can be reversibly stabilized *via* disulfide bonds. We have demonstrated in both ovarian cancer xenograft model and murine transgenic breast cancer model that these novel NPs could be used as: 1) amplifiable nanoprobes to increase the sensitivity of multimodal imaging for tumor detection, 2) nanotransducers that can be activated to generate heat and ROS efficiently at

tumor sites for PTT/PDT dual therapy via a single wavelength light, and 3) nanocarriers with programmable releasing property that can minimize the premature drug release in blood and allow efficient release upon light irradiation and/or triggered by the endogenous reducing agent present at tumor site or in cancer cells[21]. The superior imaging capability of NPs can be further utilized to monitor the real-time *in vivo* delivery of NPs and for assessing their therapeutic efficacy non-invasively. The results shown above support our concept of using an organic porphyrin nanoconstruct assembled from a single and well-defined polymer unit as a smart and extremely versatile "all-in-one" nanomedicine platform to mediate multimodality imaging (NIRFI, MRI, PET and PET-MRI), as well as PTT, PDT and targeted drug delivery. To the best of our knowledge, this is the first report of an organic nanoparticle system that is able to integrate such a broad range of smart and clinically relevant functionalities in a single nano-formulation.

The integration of additional functionality into existing nanoparticles will typically increase the cost and the complexity of synthesis, lead to more heterogeneous formulations and affect their *in vivo* performance[45]. For clinical translation, the cost-effectiveness of the nanoplatform must be carefully considered. The present multifunctional nanoporphyrins were developed based on a single and well-defined building block. The synthesis of porphyrin/cholic acid hybrid telodendrimer is highly reproducible and can be easily scaled-up to kilogram level at relatively low cost. The *in vivo* performance of NPs remains high in each of its functionality compared to the other nanoparticle systems as discussed below.

A variety of fluorescence labelled nanoparticles [7,46,47] and quantum dots[8,48] have been reported for NIRFI. However, most of these nanoparticles lacked a strategy to minimize the signal in blood and amplify the signal at tumor site. Porphysome nanovesicles have been found to have structure-dependent fluorescence properties that can be used for low-background NIRFI[7]. However, porphysome nanovesicles are relatively large (~100nm) resulting in very high uptake in RES, liver and spleen. NPs are relatively small (20-30 nm); they can be reversibly crosslinked and exhibit unique architecture-dependent fluorescence. Therefore, they are particularly suited as activatable optical nanoprobes to increase the sensitivity of NIRFI for improved cancer detection through background suppression in blood as well as preferential accumulation and signal amplification at tumor site. This latter property makes NPs particularly useful as probes for image-guided surgery. SPIO-nanoparticles [11,12] have been proposed as T_2-weighted MRI contrast agents but they often suffered from relatively low sensitivity due to their negative contrast [2,49]. Nanoparticle-based T_1-weighted MRI agents usually have excellent contrast enhancement but they often require additional steps for the ligation of chelators [4,49,50]. The NPs have intrinsic ability to chelate Gd(III) (Fig. 1d), preferentially accumulate at tumor site and possess architecture-dependent magnetic resonance property which allow them to be used as activatable contrast agents for sensitive and tumor-specific MRI. Unlike most other nanoparticles that require added chelation, NPs possess intrinsic ability to directly chelate ^{64}Cu(II) that allows not only their biodistribution but also pharmacokinetics to be noninvasively tracked *in vivo* by PET. Furthermore, NPs can chelate Gd(III) and radiotracers simultaneously, making it a promising dual-modality nano-imaging agent for combined PET-MRI. There have been studies showing that PTT has synergistic effect with PDT and could enhance the outcome of

PDT and chemotherapy by increasing local permeability of the sensitizer and drugs [40,43,44]. Here we demonstrated *in vivo* that the "soft" organic NPs could be employed for simultaneous PTT/PDT using a portable, single wavelength NIR laser. The architecture dependent photonic properties of NPs could be utilized to minimize the unintended toxicity of photosensitizers in blood, and deliver significantly higher amount of ROS and heat to tumor than comparable nanocarriers. Although NPs can in principle reach tumor sites throughout the body, PTT and PDT, however, is limited by the region of the body accessible to light irradiation and the depth of NIR laser penetration into tissues. The improvements in light delivery methods [51] and targeting property of NPs *via* targeting moieties for specific type of tumors [52] will undoubtedly further increase the therapeutic efficacy and accelerate the translation of such NPs to the clinic.

NPs can be used as a non-toxic nano-platform for hydrophobic anticancer drug formulation, yielding relatively small and monodisperse nanotherapeutics with high drug loading efficiency. To minimize premature drug release in the circulation, NPs can be crosslinked by disulfide bonds. Such crosslinked NPs can be triggered to release the drug content by light exposure and intracellular reducing agents. The current configuration of our NPs is designed to carry hydrophobic drugs. Further modifications of the NPs, however, will be needed if we want to deliver hydrophilic payloads such as DNA, RNA, proteins and enzymes.

In addition to achieving and validating the nanoscale integration of imaging and therapeutic functions, it is important to demonstrate the benefits and synergy of such a combined approach. We have demonstrated that NPs could be activated to release singlet oxygen, heat and drugs simultaneously at the tumor sites for simultaneous PTT/PDT and chemotherapy upon illumination. This synergistic approach will make PTT/PDT much more effective. For tumors that are beyond the reach of the light, anti-tumor effects can still be achieved with a chemotherapeutic agent such as paclitaxel and doxorubicin encapsulated inside the NPs. We have also shown that the unique MR imaging capabilities of NPs could be utilized to conveniently monitor the biodistribution of NPs as well as their therapeutic efficacy, including the tumor size and necrosis inside the tumor after PTT/PDT. This integrated nanomedicine platform shows great promise as a highly versatile multimodal theranostic agent against cancers.

METHODS

Synthesis of telodendrimers

The representative porphyrin/cholic acid hybrid telodendrimer (PEG^{5k}-Por_4-CA_4, Fig. 1a, Supplementary Fig. 1) was synthesized via solution-phase condensation reactions from MeO-PEG-NH_2 utilizing stepwise peptide chemistry according to our published methods[16]. Briefly, (Fmoc)Lys(Fmoc)-OH (3 eq.) was coupled onto the N terminus of PEG using DIC and HOBt as coupling reagents until a negative Kaiser test result was obtained, thereby indicating completion of the coupling reaction. PEGylated molecules were precipitated by adding cold ether and then washed with cold ether twice. Fmoc groups were removed by the treatment with 20% (v/v) 4-methylpiperidine in dimethylformamide (DMF), and the PEGylated molecules were precipitated and washed three times by cold ether. White powder precipitate was dried under vacuum and one coupling of (Fmoc)Lys(Fmoc)-OH and one

coupling of (Fmoc)lys(Boc)-OH were carried out respectively to generate a third generation of dendritic polylysine terminated with four Boc and Fmoc groups on one end of PEG. Cholic acid NHS ester [16] and pyropheophorbide-a were coupled to the terminal end of dendritic polylysine after the removal of Fmoc with 20%(v/v) 4-methylpiperidine and the removal of Boc groups with 50% (v/v) trifluoroacetic acid (TFA) in dichloromethane (DCM), respectively. The telodendrimer solution was filtered and then dialyzed against 4 L water in a dialysis tube with MWCO of 3.5 KDa; reservoir water was refreshed completely four times in 24 h. Finally, the telodendrimer was lyophilized. The molecular weight of PEG^{5k}-Por_4-CA_4 was collected on ABI 4700 MALDI TOF/TOF mass spectrometer (linear mode) using R-cyano-4-hydroxycinnamic acid as a matrix. The mono-dispersed mass traces were detected for the telodendrimers, and the molecular weight of the telodendrimer from MALDI-TOF MS (Supplementary Fig. 2) was almost identical to the theoretical value. ^1H NMR spectra of the telodendrimers were recorded on an Avance 500 Nuclear Magnetic Resonance Spectrometer (Bruker) using DMSO-d6 and D2O as solvents. The concentration of the telodendrimers was kept at 5×10^{-4} M for NMR measurements (Supplementary Fig. 3).

The thiolated pyropheophorbide-a telodendrimer (named as PEG^{5k}-Cys_4-Por_4-CA_4, Fig. 2a, Supplementary Fig. 10) was synthesized by replacing 4 of the 8 cholic acids of our previously reported thiolated telodendrimer (PEG^{5k}-Cys_4-L_8-CA_8)using the same strategy[16,21]. The typical procedure for synthesis of PEG^{5k}-Cys_4-Por_4-CA_4 was as follows: (Fmoc)Lys(Fmoc)-OH (3 eq.) was coupled onto the N terminus of PEG using DIC and HOBt as coupling reagents until a negative Kaiser test result was obtained, thereby indicating completion of the coupling reaction. PEGylated molecules were precipitated by adding cold ether and then washed with cold ether twice. Fmoc groups were removed by the treatment with 20%(v/v) 4-methylpiperidine in dimethylformamide (DMF), and the PEGylated molecules were precipitated and washed three times by cold ether. White powder precipitate was dried under vacuum and one coupling of (Fmoc)Lys(Fmoc)-OH and one coupling of (Dde)lys(Fmoc)-OH were carried out respectively to generate a third generation of dendritic polylysine terminated with four Dde and Fmoc groups on one end of PEG. Then the Fmoc groups were removed. (Fmoc)Cys(Trt)-OH, (Fmoc)Ebes-OH and Cholic acid NHS ester (12 eq.) were coupled step by step to the terminal end of dendritic polylysine. After the removal of Dde protecting group by 2%(v/v) hydrazine in DMF, (Fmoc)Ebes-OH and pyropheophorbide-a (12 eq.) were coupled subsequently to the leftover amino groups on the terminal end of dendritic polylysine. The Trt groups on cysteines were removed by TFA/H2O/ethanedithiol (EDT)/triethylsilane (TIS) (94:2.5:2.5:1, v/v) resulting in PEG^{5k}-Cys_4-Por_4-CA_4 thiolated telodendrimer (Fig. 2a, Supplementary 10). The thiolated telodendrimer was recovered from the mixture by three cycles of dissolution/reprecipitation with DMF and ether, respectively. Finally, the thiolated telodendrimer was dissolved in acetonitrile/water and lyophilized. The molecular weight of PEG^{5k}-Cys_4-Por_4-CA_4 was collected on ABI 4700 MALDI TOF/TOF mass spectrometer (linear mode) using R-cyano-4-hydroxycinnamic acid as a matrix. The mono-dispersed mass traces were detected for the starting PEG and the telodendrimers, and the molecular weights of the telodendrimers from MALDI-TOF MS (Supplementary Fig. 11) were almost identical to the theoretical value.

Preparation of nanoporphyrins

20 mg thiol free porphyrin-telodendrimer was dissolved in 1 mL phosphate buffered saline (PBS) followed by sonication for 10 min to form NPs. In order to make CNP, 20 mg total amount of $PEG^{5k}-Cys_4-Por_4-CA_4$ was dissolved in 1 mL phosphate buffered saline (PBS) to form micelles and then sonicated for 10 min. The thiol groups on the telodendrimer were oxidized to form disulfide linkages by air[21].

Generation of metallic nanoporphyrins

To generate telodendrimers with a chelated metal, excess free metal ions were incubated with telodendrimers in methanol/chloroform for 1-5 hrs under nitrogen according to previously reported methods [7,53]. Free metal was removed by column filtration with a molecular weight cut off of 3,500. The metal-telodendrimer was then aliquoted and dried. Metallic NPs were generated by dissolving the metal-telodendrimer in PBS with sonication.

Preparation of drug loaded nanoporphyrins

Hydrophobic drugs, such as doxorubicin (DOX), were loaded into NPs by the solvent evaporation method[21,24]. Before the encapsulation of DOX into NPs, DOX·HCl was stirred with 3 molar equivalent of triethylamine in chloroform ($CHCl_3$)/methanol (MeOH) (1:1, v/v) overnight to remove HCl from DOX·HCl. 20 mg porphyrintelodendrimer along with different amount of neutralized DOX were first dissolved in $CHCl_3$/MeOH, mixed, and evaporated on rotavapor to obtain a homogeneous dry polymer film. The film was reconstituted in 1 mL phosphate buffered solution (PBS), followed by sonication for 30 min, allowing the sample film to disperse into NP solution. Finally, the NP solution was filtered with 0.22 μm filter to sterilize the sample. To determine the amount of drugs, drug-loaded nanoporphyrins were diluted with DMSO (NP solution/DMSO: 1:9, v/v) to dissociate nanoparticles. The drug loading was analyzed on a HPLC system (Waters), wherein calibration curve was obtained using a series of drug/DMSO standard solutions with different concentrations. The drug loaded CNPs were prepared via the same method followed the oxidation of the thiols to form intramicellar disulfide bonds[21].

Characterizations of nanoporphyrins

The size and size distribution of NPs were measured by dynamic light scattering (DLS) instruments (Microtrac). The concentrations were kept at 1.0 mg/mL for DLS measurements. All measurements were performed at 25 °C, and data were analyzed by Microtrac FLEX Software 10.5.3. The morphology of NPs was observed on a Philips CM-120 transmission electron microscope (TEM). Briefly, the aqueous nanoparticle solution (1.0 mg/mL) was deposited onto copper grids, with or without staining by phosphotungstic acid (PTA) for 2 seconds, and measured at room temperature. The size of the particles was analyzed by TEM software (DigitalMicrograph, Gatan, Inc). The absorbance and the fluorescence signal of NPs were measured on a fluorescence spectrometry (SpectraMax M2, Molecular Devices, Sunnyvale, CA). The near infrared fluorescence of NP solutions (10μL) was scanned using a Kodak multimodal imaging system IS2000MM. The thermo property of NP solutions (10μL) was studies using a FLIR thermal camera. The ROS production of NPs was studied using Singlet oxygen sensor green

(SOSG) or 2',7'-Dichlorofluorescin diacetate (DCF-DA) as an indicator and compared with PBS. Briefly, SOSG and/or DCF-DA working solution was mixed with different concentration of NPs/CNPs with and without SDS (2.5 mg/mL) and GSH (10 mM) in 96-well plate. After 20 seconds of NIF light exposure, green fluorescence was monitored by micro-plate reader (SpectraMax M2, Molecular Devices, Sunnyvale, CA).

Stability of nanoporphyrins in SDS and human plasma

The stability study was performed to monitor the change in fluorescence and particle size of NPs and CNPs in the presence of sodium dodecyl sulfate (SDS), which was reported to be able to efficiently break down polymeric micelles [54]. An SDS solution (7.5 mg/mL) was added to aqueous solutions of NPs (1.5 mg/mL). The final SDS concentration was 2.5 mg/mL and the micelle concentration was kept at 1.0 mg/mL. The fluorescence signal of the solutions was measured on micro-plate reader (SpectraMax M2). The size and size distribution of the NP solutions was monitored at predetermined time intervals by DLS. The stability of the micelles was also evaluated in the presence of glutathione (GSH, 20 mM) together with SDS. The stability of DOX-loaded NPs was further studied in 50% (v/v) plasma from healthy human volunteers. The mixture was incubated at physiological body temperature (37 °C) followed by size measurements at predetermined time intervals up to 48 hrs.

DOX release in human plasma

CNP-DOX solutions were prepared to determine the *in vitro* drug release profile in plasma. The initial DOX concentration was 1.0 mg/mL while the CNP concentration was 10 mg/mL. CNP alone and our reported standard micelles (without porphyrins) with DOX at the same drug content were also prepared for comparison. When DOX was encapsulated in the core of CNPs, the proximity between DOX and Por was within the FRET range allowing efficient energy transfer from DOX to Por molecules upon excitation of DOX at 480 nm (**Fig 2e,f**). Upon excitation at 480 nm, the signal of CNPs alone was much smaller in comparison with the corresponding FRET signal. Therefore, by monitoring the dynamic change of FRET ratio, we were able to monitor the release of DOX from CNPs in real time. Aliquots of these nanoparticle solutions were diluted 9 times by human plasma and incubated in an incubator at 37 °C with a stirring speed of 100 rpm. The fluorescence spectra of these nanoparticle solutions were measured by NanoDrop spectrophotometer (Thermo Scientific) at pre-determined time points. The *in vitro* DOX release profiles from CNPs were further measured by the dialysis method[21]. In some experiments, aliquots of DOX-loaded nanoporphyrin solution were pre-treated with light or GSH (10 mM) or no treatment and then dialyzed against diluted human plasma. The concentration of DOX at different time points were measured using a Molecular Devices SpectraMax M2 (Sunnyvale, CA) at excitation 470 nm/emission 590 nm. Data were reported as the average percentage of DOX accumulative release for each triplicate sample.

In vitro cell uptake and cytotoxicity

To study the intracellular delivery of DOX loaded nanoporphyrins, SKOV3 ovarian cancer cells were seeded on 8 well chamber slides and treated with CNP-DOX (0.1 mg/mL DOX)

in solution containing Hoechst 33342 for 2 hrs. Cell imaging was acquired using Deltavision deconvolution microscope. SKOV3 ovarian cancer cell lines were used to evaluate the photosensitizing function of CNPs. We first treated the cancer cells with various concentrations of CNPs or 5-aminolevulinic acid (5-ALA), the traditional photodynamic diagnosis/therapy agent, for 24 hrs. After thorough washing, the cells were exposed to NIF light as indicated. Cell viability was determined using WST-8 proliferation kit 24 hrs after illumination. In another experiments, CNPs or DOX loaded CNPs, free DOX, and DOX loaded crosslinked micelles (without porphyrins)[21] were used to treat the cancer cells for 24 hrs. After three times of wash, cells were illuminated with light for 1 minute. Cell viability was determined by WST-8 after 24 hrs of incubation.

ROS production and cell death mechanisms

We firstly treated SKOV3 cells with or without 10 μg/mL of CNPs for 24 hrs followed by 30 minute loading with DCF-DA in 96 well plate to monitor the ROS production. Cells were washed three times with PBS and replaced with fresh medium. A portion of the well was illuminated with NIR light and cell imaging was acquired under fluorescence microscope using Metamorph program. Next, to evaluate the loss of mitochondria membrane potential (Ψm) after pre-treated SKOV3 cells with NPs, we loaded cells with 40nM of $DiOC_6(3)$ for 20 minutes and a portion of the well was illuminated with NIR light. Twenty-four hours later, cells were labeled with propridium iodide (PI, dead cells) and Hoechst 33342 (nucleus), and imaging was acquired by fluorescence microscope. Last, to investigate the cellular responses to CNPs and photo-therapy, we evaluated the caspase 3/7 activity, which served as marker for a part of apoptosis pathway activation. SKOV3 cells were treated with or without 10 μg/mL CNPs for 24 hrs. After wash, cells were exposed without light or light for 0.5, 1 and 2 minutes. After 24 hrs of incubation, caspase3/7 activity was measured by adding another 50 μL of working solution for another 45 minutes. The plate was read by micro-plate reader (SpectraMax M2). Lastly, for morphology study, SKOV3 cells were cultured on 8-well chamber slides and treated with or without CNPs for 24 hrs. Two hours after treatment with light, the slide was stained with Hema3® and observed under light microscope.

Animal models

Female athymic nude mice (Nu/Nu strain), 6-8 weeks age, were purchased from Harlan (Livermore, CA). All animal experiments were performed in compliance with institutional guidelines and according to protocol No. 07-13119 and No. 09-15584 approved by the Animal Use and Care Administrative Advisory Committee at the University of California, Davis. The subcutaneous xenograft model of ovarian cancer was established by injecting 2×10^6 SKOV3 ovarian cells in a 100 μL of mixture of PBS and Matrigel (1:1 v/v) subcutaneously into the right flank of female nude mice. Transgenic mice with mammary cancer (FVB/n Tg(MMTV-PyVmT)) were ordered from Jackson Laboratory. Those mice were known to spontanously developed mammary cancers at ages of 4-40 months.

In vivo blood elimination kinetics

The jugular vein of male Sprague-Dawley rats was cannulated and a catheter was implanted for intravenous injection and blood collection (Harland, Indianapolis, IN). NPs and CNPs at

identical porphyrin concentration were injected through the catheter at a dose of 5mg/kg body weight (n=3 for each group). Whole blood samples (approximately 100 μL) were collected via jugular vein catheter before dosing and at pre-determined time points post-injection and used to detect porphyrin concentration by the measurement of absorbance at 680 nm on micro-plate reader (SpectraMax M2). The values were plotted versus time after the subtraction of blood background.

NIRF imaging

After transgenic mice (10-12 weeks) and nude mice developed established tumors (6-10 mm in diameter), they were subjected to *in vivo* NIRF imaging by injecting 100 μL of NPs via tail vein. At different time points post-injection of NPs, mice were scanned using a Kodak multimodal imaging system IS2000MM with an excitation bandpass filter at 625/20 nm and an emission at 700/35 nm under anaesthesia. After *in vivo* imaging, animals were euthanized. Tumors and major organs were excised and imaged with the Kodak imaging station. To monitor the kinetics of biodistribution at the tissue level, SKOV3 tumor-bearing mice were given 100 μL of CNPs via tail vein and euthanized at 1, 24, or 48 hrs. Right before euthanasia, Dextran-FITC solution was injected intravenously to locate blood vessel. Tumors were harvested and fixed in the cold formalin on ice. A fresh cross-section was made for Large-Scale-Imaging (LSI) laser scanning confocal microscope imaging. Additionally, lungs with metastatic lesions were also collected from older transgenic mice (20-24 weeks) and fixed in cold formalin for one hour. The lung surface was imaged by LSI laser scanning confocal microscopy. After imaging, lungs were subjected to histopathological evaluation. In some cases, the blood of the mice were drawn and measured at predetermined time points.

Radiolabeling

$^{64}CuCl_2$ in 0.1 M HCl (Washington University, MO) was buffered with 1.0 M ammonium acetate to pH 7. PEG^{5k}-Por_4-CA_4 telodendrimer was dissolved in methanol before adding a small volume of buffered $^{64}CuCl_2$. The radiolabeling solution was incubated for 30 min at room temperature. The methanol was evaporated and the film of telodendrimers was rehydrated with PBS to generate ^{64}Cu labeled NPs. Free ^{64}Cu was removed by centrifuged filtration using 3500 kDa cutoff Amicon centrifugal filter units (Millipore, Billerica, MA), or alternatively, Micro Bio-Spin 6 columns (Bio-Rad, Hercules, CA). Radiochemical purity and yield were assessed using instant thin-layer chromatography (ITLC). To prepare dual-labeled Gd/^{64}Cu NPs, pre-prepared Gdtelodendrimer was added to ^{64}Cu-PEG^{5k}-Por_4-CA_4 telodendrimer radiolabeling solution in methanol, followed by drying, reconstitution in PBS, and purification.

MRI and PET imaging

The *in vitro* MRI signal enhancement of Gd-NPs in the absence and in the presence of SDS was obtained using a Bruker Biospec 7T MRI scanner using T1-weighted Fast Low Angle SHot (FLASH) sequence (echo time (TE)/repetition time (TR) = 4/200 ms) using a 128 × 128 matrix size. Nude mice bearing SKOV3 ovarian cancer xenograft, nude mice bearing A549 lung cancer xenografts and transgenic mice with mammary cancer (FVB/n

Tg(MMTV-PyVmT) were imaged on a Bruker Biospec 7T MRI scanner. Spin echo images were acquired to determine solid tumor location and volume. To assess the kinetics of the Gd-NPs in the body and tumor as well as the nanoparticle-enhanced MRI signal intensity, a dynamic T1-weighted FLASH sequence was used to acquire images just before injection and at predetermined time points post-injection of Gd-NPs (Gd dose: Gd dose: 0.015-0.02 mmole/kg) (TE/TR = 4/200 ms) using a 128×128 matrix size. MRI was also used to monitor the tumor growth in nude mice bearing SKOV3 ovarian cancer xenografts before and after PTT/PDT using the same parameters. PET was performed on nude mice bearing SKOV3 ovarian cancer xenografts post-injection of ^{64}Cu-labeled NPs (described in Supplementary Methods) (150-200 μL, ^{64}Cu dose: 0.6-0.8 mCi) on a small-animal microPET system (Siemens Inveon D-PET). PET-MRI was performed on a small-animal microPET system (Siemens Inveon D-PET) and a Bruker Biospec 7T MRI scanner. Nude mice bearing A549 lung cancer xenografts were placed on a movable bed that fits into both scanners in order to facilitate co-registration of the PET and MR images. After tail vein injection of ^{64}Cu and Gd dual-labeled NPs (described in Supplementary Methods) (150-200 μL, ^{64}Cu dose: 0.6-0.8 mCi, Gd dose: 0.015-0.02 mmole/kg), the mice were imaged under anesthesia (2% isoflurane in oxygen at 2L/min) at 4 or 24 hrs post-injection. Amide software was used to co-register the PET and MR images.

In vivo therapeutic studies

Transgenic mice with mammary cancer (FVB/n Tg(MMTV-PyVmT) and nude mice bearing SKOV3 ovarian cancer xenograft were used for the *in vivo* therapeutic studies. When tumor volumes reached 4-5 mm in transgenic mice, CNPs with and without 2.5 mg/kg DOX were injected via tail vein once per week for 3 doses. After 24 hrs, tumors were illuminated with a diode laser system (Applied Optronics, Newport, CT) at 690 nm under general anaesthesia. The light dose was 1.25 W cm^{-2} for 2 minutes through an optical fiber producing a 0.8 cm^2 beam spot to cover the whole tumor. Tumor surface temperatures were monitored with thermal camera (FLIR). The temperature readings in the central point of the illumination area were recorded continuously. Intratumoral ROS production after irradiation was measured using DCF-DA and/or SOSG as indicators. In some cases, the blood of the mice was drawn and the ROS and heat production in blood after irradiation were measured at predetermined time points. The hemolysis was also followed. Tumor volume was measured twice a week and mice were sacrificed once tumor size reached 1000 mm^3. Tumors were harvested for histopathological evaluation 24 hours post-irradiation. The SKOV3 ovarian cancer xenograft model was established by injecting one million cells subcutaneously at lower flank area. After tumors reached 150-200 mm^3, mice received PBS, 2.5 mg/kg DOX, and CNPs with and without 2.5 mg/kg DOX every 3 days for 3 doses. 0.2 W cm^{-2} of laser light was given for 2 min after dose 1 and 3. Tumor sizes and body weight were measured twice a week, while mice were monitored daily for potential signs of toxicity. Two days after the last dose, CBC and serum chemistry were performed. One mouse from each group was also sacrificed and major organs were harvested for histopathology evaluation.

Statistical analysis

Statistical analysis was performed by Student's *t*-test for two groups, and one-way ANOVA for multiple groups. All results were expressed as the mean ± standard deviation (SD) unless otherwise noted. A value of P<0.05 was considered statistically significant.

Supplementary Material

Refer to Web version on PubMed Central for supplementary material.

REFERENCES

1. Lee DE, et al. Multifunctional nanoparticles for multimodal imaging and theragnosis. Chem Soc Rev. 2012; 41:2656–2672. [PubMed: 22189429]

2. Xie J, Lee S, Chen X. Nanoparticle-based theranostic agents. Adv Drug Deliv Rev. 2010; 62:1064–1079. [PubMed: 20691229]

3. Choi KY, Liu G, Lee S, Chen X. Theranostic nanoplatforms for simultaneous cancer imaging and therapy: current approaches and future perspectives. Nanoscale. 2012; 4:330–342. [PubMed: 22134683]

4. Luk BT, Fang RH, Zhang L. Lipid- and polymer-based nanostructures for cancer theranostics. Theranostics. 2012; 2:1117–1126. [PubMed: 23382770]

5. Pan D. Theranostic nanomedicine with functional nanoarchitecture. Mol Pharm. 2013; 10:781–782. [PubMed: 23452025]

6. Chen X, Gambhir SS, Cheon J. Theranostic nanomedicine. Acc Chem Res. 2011; 44:841. [PubMed: 22004477]

7. Lovell JF, et al. Porphysome nanovesicles generated by porphyrin bilayers for use as multimodal biophotonic contrast agents. Nat Mater. 2011; 10:324–332. [PubMed: 21423187]

8. Qi L, Gao X. Emerging application of quantum dots for drug delivery and therapy. Expert opinion on drug delivery. 2008; 5:263–267. [PubMed: 18318649]

9. Mahmoudi M, Sant S, Wang B, Laurent S, Sen T. Superparamagnetic iron oxide nanoparticles (SPIONs): development, surface modification and applications in chemotherapy. Adv Drug Deliv Rev. 2011; 63:24–46. [PubMed: 20685224]

10. Laurent S, et al. Magnetic iron oxide nanoparticles: synthesis, stabilization, vectorization, physicochemical characterizations, and biological applications. Chem Rev. 2008; 108:2064–2110. [PubMed: 18543879]

11. Demberelnyamba D, Ariunaa M, Shim YK. Newly synthesized water soluble cholinium-purpurin photosensitizers and their stabilized gold nanoparticles as promising anticancer agents. Int J Mol Sci. 2008; 9:864–871. [PubMed: 19325790]

12. von Maltzahn G, et al. Computationally guided photothermal tumor therapy using long-circulating gold nanorod antennas. Cancer Res. 2009; 69:3892–3900. [PubMed: 19366797]

13. Singh N, Jenkins GJ, Asadi R, Doak SH. Potential toxicity of superparamagnetic iron oxide nanoparticles (SPION). Nano reviews. 2010; 1

14. Cheng L, Yang K, Chen Q, Liu Z. Organic stealth nanoparticles for highly effective in vivo near-infrared photothermal therapy of cancer. ACS Nano. 2012; 6:5605–5613. [PubMed: 22616847]

15. Cabral H, et al. Accumulation of sub-100 nm polymeric micelles in poorly permeable tumours depends on size. Nature nanotechnology. 2011; 6:815–823.

16. Luo J, et al. Well-defined, size-tunable, multifunctional micelles for efficient paclitaxel delivery for cancer treatment. Bioconjug Chem. 2010; 21:1216–1224. [PubMed: 20536174]

17. Chauhan VP, et al. Normalization of tumour blood vessels improves the delivery of nanomedicines in a size-dependent manner. Nat Nanotechnol. 2012; 7:383–388. [PubMed: 22484912]

18. Zhou K, et al. Multicolored pH-tunable and activatable fluorescence nanoplatform responsive to physiologic pH stimuli. J Am Chem Soc. 2012; 134:7803–7811. [PubMed: 22524413]

19. Li Y, et al. Probing of the assembly structure and dynamics within nanoparticles during interaction with blood proteins. ACS nano. 2012; 6:9485–9495. [PubMed: 23106540]

20. Wu DQ, et al. Porphyrin and galactosyl conjugated micelles for targeting photodynamic therapy. Pharmaceutical research. 2010; 27:187–199. [PubMed: 19888639]

21. Li Y, et al. Well-defined, reversible disulfide cross-linked micelles for on-demand paclitaxel delivery. Biomaterials. 2011; 32:6633–6645. [PubMed: 21658763]

22. Xiao K, et al. The effect of surface charge on in vivo biodistribution of PEG-oligocholic acid based micellar nanoparticles. Biomaterials. 2011; 32:3435–3446. [PubMed: 21295849]

23. Li Y, et al. Well-defined, reversible boronate crosslinked nanocarriers for targeted drug delivery in response to acidic pH values and cis-diols. Angew Chem Int Ed Engl. 2012; 51:2864–2869. [PubMed: 22253091]

24. Li Y, et al. A novel size-tunable nanocarrier system for targeted anticancer drug delivery. Journal of Controlled Release. 2010; 144:314–323. [PubMed: 20211210]

25. Kato J, et al. Disulfide cross-linked micelles for the targeted delivery of vincristine to B-cell lymphoma. Mol Pharm. 2012; 9:1727–1735. [PubMed: 22530955]

26. Rong P, et al. Photosensitizer loaded nano-graphene for multimodality imaging guided tumor photodynamic therapy. Theranostics. 2014; 4:229–239. [PubMed: 24505232]

27. Ng KK, Lovell JF, Vedadi A, Hajian T, Zheng G. Self-assembled porphyrin nanodiscs with structure-dependent activation for phototherapy and photodiagnostic applications. ACS Nano. 2013; 7:3484–3490. [PubMed: 23464857]

28. Matsumoto S, et al. Environment-responsive block copolymer micelles with a disulfide cross-linked core for enhanced siRNA delivery. Biomacromolecules. 2009; 10:119–127. [PubMed: 19061333]

29. Xiao K, et al. PEG-oligocholic acid telodendrimer micelles for the targeted delivery of doxorubicin to B-cell lymphoma. Journal of Controlled Release. 2011; 155:272–281. [PubMed: 21787818]

30. Bui T, et al. Novel Gd nanoparticles enhance vascular contrast for high-resolution magnetic resonance imaging. PLoS One. 2010; 5

31. Judenhofer MS, et al. Simultaneous PET-MRI: a new approach for functional and morphological imaging. Nat Med. 2008; 14:459–465. [PubMed: 18376410]

32. Catana C, et al. Simultaneous in vivo positron emission tomography and magnetic resonance imaging. Proc Natl Acad Sci U S A. 2008; 105:3705–3710. [PubMed: 18319342]

33. Torres Martin de Rosales R, et al. Synthesis of 64Cu(II)-bis(dithiocarbamatebisphosphonate) and its conjugation with superparamagnetic iron oxide nanoparticles: in vivo evaluation as dual-modality PET-MRI agent. Angew Chem Int Ed Engl. 2011; 50:5509–5513. [PubMed: 21544908]

34. Choi JS, et al. A hybrid nanoparticle probe for dual-modality positron emission tomography and magnetic resonance imaging. Angew Chem Int Ed Engl. 2008; 47:6259–6262. [PubMed: 18613191]

35. Lee HY, et al. PET/MRI dual-modality tumor imaging using arginine-glycine-aspartic (RGD)-conjugated radiolabeled iron oxide nanoparticles. J Nucl Med. 2008; 49:1371–1379. [PubMed: 18632815]

36. Agostinis P, et al. Photodynamic therapy of cancer: an update. CA Cancer J Clin. 2011; 61:250–281. [PubMed: 21617154]

37. Jin CS, Lovell JF, Chen J, Zheng G. Ablation of hypoxic tumors with dose-equivalent photothermal, but not photodynamic, therapy using a nanostructured porphyrin assembly. ACS Nano. 2013; 7:2541–2550. [PubMed: 23394589]

38. Wang J, et al. Assembly of aptamer switch probes and photosensitizer on gold nanorods for targeted photothermal and photodynamic cancer therapy. ACS Nano. 2012; 6:5070–5077. [PubMed: 22631052]

39. Kuo WS, et al. Gold nanomaterials conjugated with indocyanine green for dual-modality photodynamic and photothermal therapy. Biomaterials. 2012; 33:3270–3278. [PubMed: 22289264]

40. Jang B, Park JY, Tung CH, Kim IH, Choi Y. Gold nanorod-photosensitizer complex for near-infrared fluorescence imaging and photodynamic/photothermal therapy in vivo. ACS nano. 2011; 5:1086–1094. [PubMed: 21244012]

41. O'Neal DP, Hirsch LR, Halas NJ, Payne JD, West JL. Photo-thermal tumor ablation in mice using near infrared-absorbing nanoparticles. Cancer Lett. 2004; 209:171–176. [PubMed: 15159019]

42. Bardhan R, Lal S, Joshi A, Halas NJ. Theranostic nanoshells: from probe design to imaging and treatment of cancer. Acc Chem Res. 2011; 44:936–946. [PubMed: 21612199]

43. Tian B, Wang C, Zhang S, Feng L, Liu Z. Photothermally enhanced photodynamic therapy delivered by nano graphene oxide. ACS nano. 2011; 5:7000–7009. [PubMed: 21815655]

44. Shi SG, et al. Photothermally enhanced photodynamic therapy based on mesoporous Pd@Ag@mSiO(2) nanocarriers. J Mater Chem B. 2013; 1:1133–1141.

45. Cheng Z, Al Zaki A, Hui JZ, Muzykantov VR, Tsourkas A. Multifunctional nanoparticles: cost versus benefit of adding targeting and imaging capabilities. Science. 2012; 338:903–910. [PubMed: 23161990]

46. Yang Z, et al. Long-circulating near-infrared fluorescence core-cross-linked polymeric micelles: synthesis, characterization, and dual nuclear/optical imaging. Biomacromolecules. 2007; 8:3422–3428. [PubMed: 17958440]

47. Yang H, et al. Micelles assembled with carbocyanine dyes for theranostic near-infrared fluorescent cancer imaging and photothermal therapy. Biomaterials. 2013; 34:9124–9133. [PubMed: 24008037]

48. Michalet X, et al. Quantum dots for live cells, in vivo imaging, and diagnostics. Science. 2005; 307:538–544. [PubMed: 15681376]

49. Zhu D, Liu F, Ma L, Liu D, Wang Z. Nanoparticle-based systems for t1-weighted magnetic resonance imaging contrast agents. Int J Mol Sci. 2013; 14:10591–10607. [PubMed: 23698781]

50. Jeong SY, et al. Biocompatible Polyhydroxyethylaspartamide-based Micelles with Gadolinium for MRI Contrast Agents. Nanoscale Res Lett. 2010; 5:1970–1976. [PubMed: 21170410]

51. Idris NM, et al. In vivo photodynamic therapy using upconversion nanoparticles as remote-controlled nanotransducers. Nat Med. 2012; 18:1580–1585. [PubMed: 22983397]

52. Xiao K, et al. "OA02" peptide facilitates the precise targeting of paclitaxel-loaded micellar nanoparticles to ovarian cancer in vivo. Cancer Res. 2012; 72:2100–2110. [PubMed: 22396491]

53. Kim JK, et al. Gadolinium-chlorin is potentially a new tumor specific MRI contrast agent. Arch Pharm Res. 2006; 29:188–190. [PubMed: 16596988]

54. Koo AN, et al. Disulfide-cross-linked PEG-poly(amino acid)s copolymer micelles for glutathione-mediated intracellular drug delivery. Chemical Communications. 2008:6570–6572. [PubMed: 19057782]
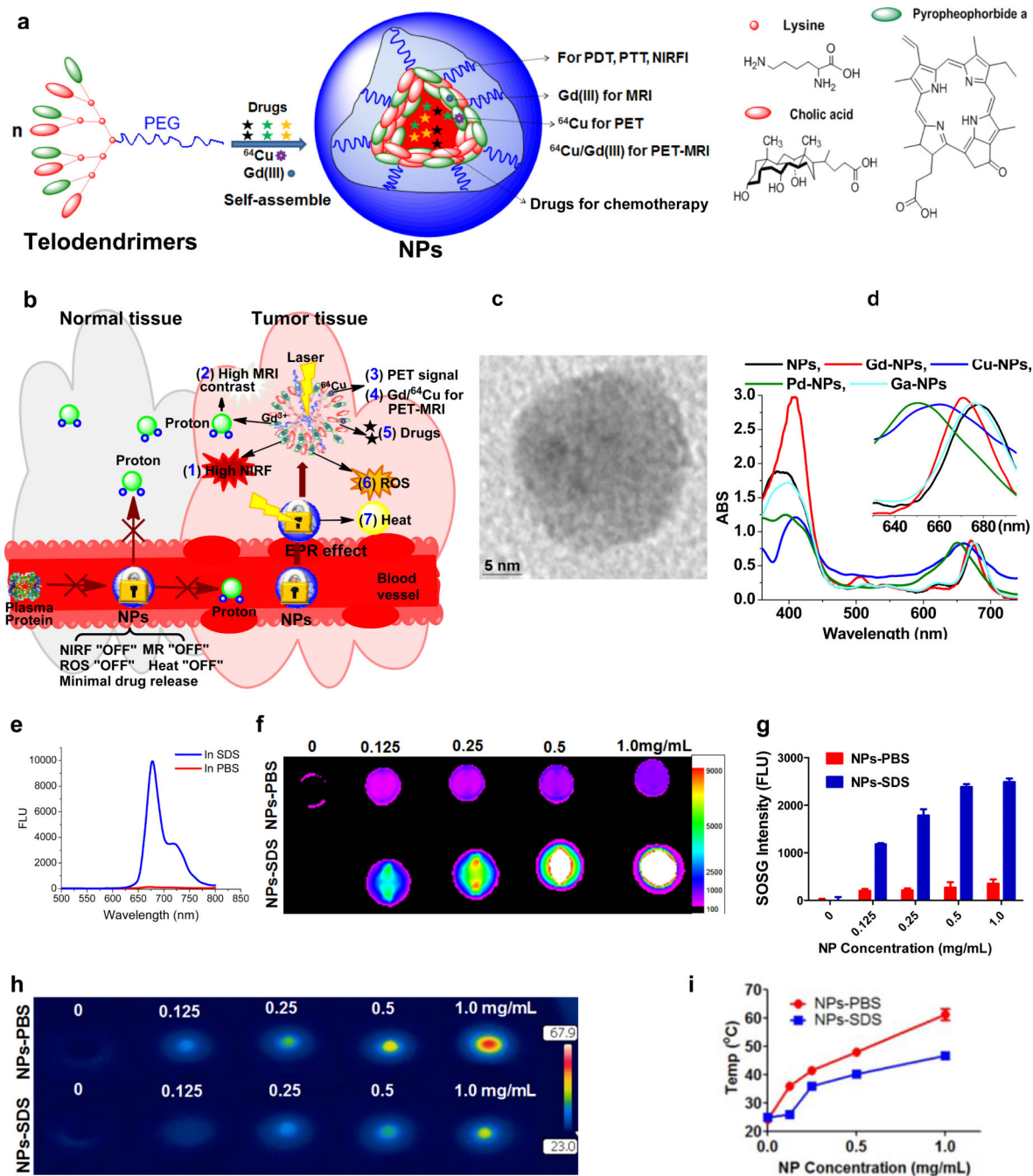
Figure 1. Design, synthesis and characterizations of nanoporphyrins
(**a**) Schematic illustration of a multifunctional nanoporphyrin self-assembled by a representative porphyrin- telodendrimer, PEG^{5k}-Por_4-CA_4, comprised of 4 pyropheophorbide-a molecules and 4 cholic acids attached to the terminal end of a linear PEG chain. (**b**) Schematic illustration of nanoporphyrins as a smart "all-in-one" nanomedicine platform against cancers. (**c**) TEM image of nanoporphyrins (stained with phosphotungstic acid, PTA). (**d**) The absorbance spectra of NPs before and after chelating different metal ions. (**e**) Fluorescence emission spectra of NPs in the presence of PBS (red)

and SDS (blue). Excitation: 405 nm. **(f)** Near-infrared fluorescence imaging of nanoporphyrin solution (10 µL) in the absence and in the presence of SDS with an excitation bandpass filter at 625/20 nm and an emission filter at 700/35 nm. **(g)** Single oxygen generation of NPs in PBS and SDS upon light irradiation (690 nm at 0.25 w/cm^2 for 60 seconds) measured by using SOSG as an indicator[26,27] (n=3). Concentration-dependent photo-thermal transduction of NPs: **(h)** thermal images and **(i)** quantitative temperature change curve (n=2). The temperature of nanoporphyrin solution (10 µL) in the absence and in the presence of SDS was monitored by a thermal camera after irradiation with NIR laser (690 nm) at 1.25 w/cm^2 for 20 seconds.
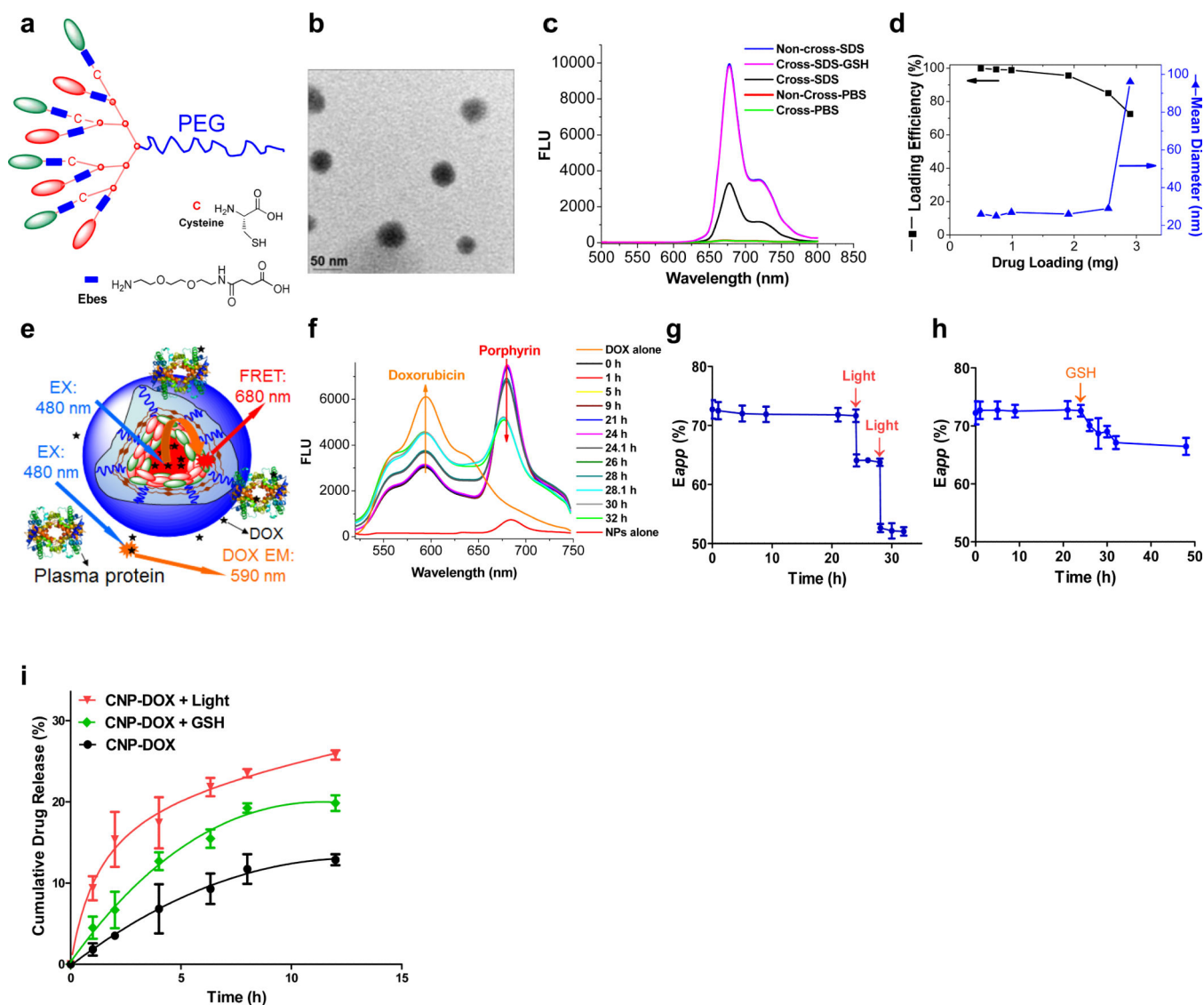
Figure 2. Design, synthesis and characterizations of disulfide crosslinked nanoporphyrins
Schematic illustration of a representative crosslinkable porphyrin-telodendrimer (PEG^{5k}-Cys$_4$-Por$_4$-CA$_4$), comprised of 4 cysteines, 4 pyropheophorbide-a molecules and 4 cholic acids attached to the terminal end of a linear PEG chain. Ebes was used as a spacer[21]. (**b**) TEM imaging of the disulfide crosslinked nanoporphyrins (CNPs) (stained with PTA). (**c**) The fluorescence emission spectra of the CNPs in the presence of PBS and SDS in the comparison with the non-crosslinked NPs. Glutathione (GSH) was used as a reducing agent to break the disulfide crosslinking[21]. Excitation: 405 nm. These CNPs also showed very weak red fluorescence emission with a peak value at 680 nm when excited at 405 nm (green curve). When the fluorescence emission spectra of the CNPs were recorded in the presence of SDS, there was increase in the peak emission at 680 nm (black curve). However, the peak value was significantly lower than that of the non-crosslinked NPs in the presence of SDS at the same porphyrin concentration. Upon addition of GSH, the CNPs were completely broken down and the peak at 680 nm in the fluorescence emission spectra increased further

to a similar value as that of NPs in the presence of SDS (pink curve). (**d**) The loading efficiency of doxorubicin into CNPs and size change of doxorubicin loaded CNPs (CNP-DOX) versus the level of drug loading. The loading efficiency is defined as the ratio of drug loaded into nanoparticles to the initial drug content. The volume of the final NP solution was kept at 1 mL and the final concentration of the telodendrimer was 20 mg/mL. (**e**) Schematic illustration of FRET-based approach for study of the real-time release of doxorubicin from nanoporphyrins in human plasma. FRET signal (**f**) and changes in apparent FRET efficiency (E_{app}) (**g**) of CNP-DOX in human plasma with irradiation at 24 hrs and 28 hrs, respectively. Irradiation: 1.25 w/cm^2 for 5 min. The apparent FRET efficiency reflects the distance between the FRET pair and is calculated as $E_{app} = I_A/(I_A + I_D)$, where I_A and I_D represent acceptor and donor intensities, respectively[19]. (**h**) Changes in apparent FRET efficiency (E_{app}) of CNP-DOX in human plasma treated with GSH (10mM) at 24 hrs. (**i**) Cumulative DOX release profiles from CNP-DOX measured by dialysis method at 37 °C. Aliquots of CNP-DOX solution were pre-treated with light (1.25W/cm^2, 5 mins) or GSH (10 mM) or no treatment and then dialyzed against diluted human plasma. Data were reported as the average percentage of DOX accumulative release for each triplicate sample.
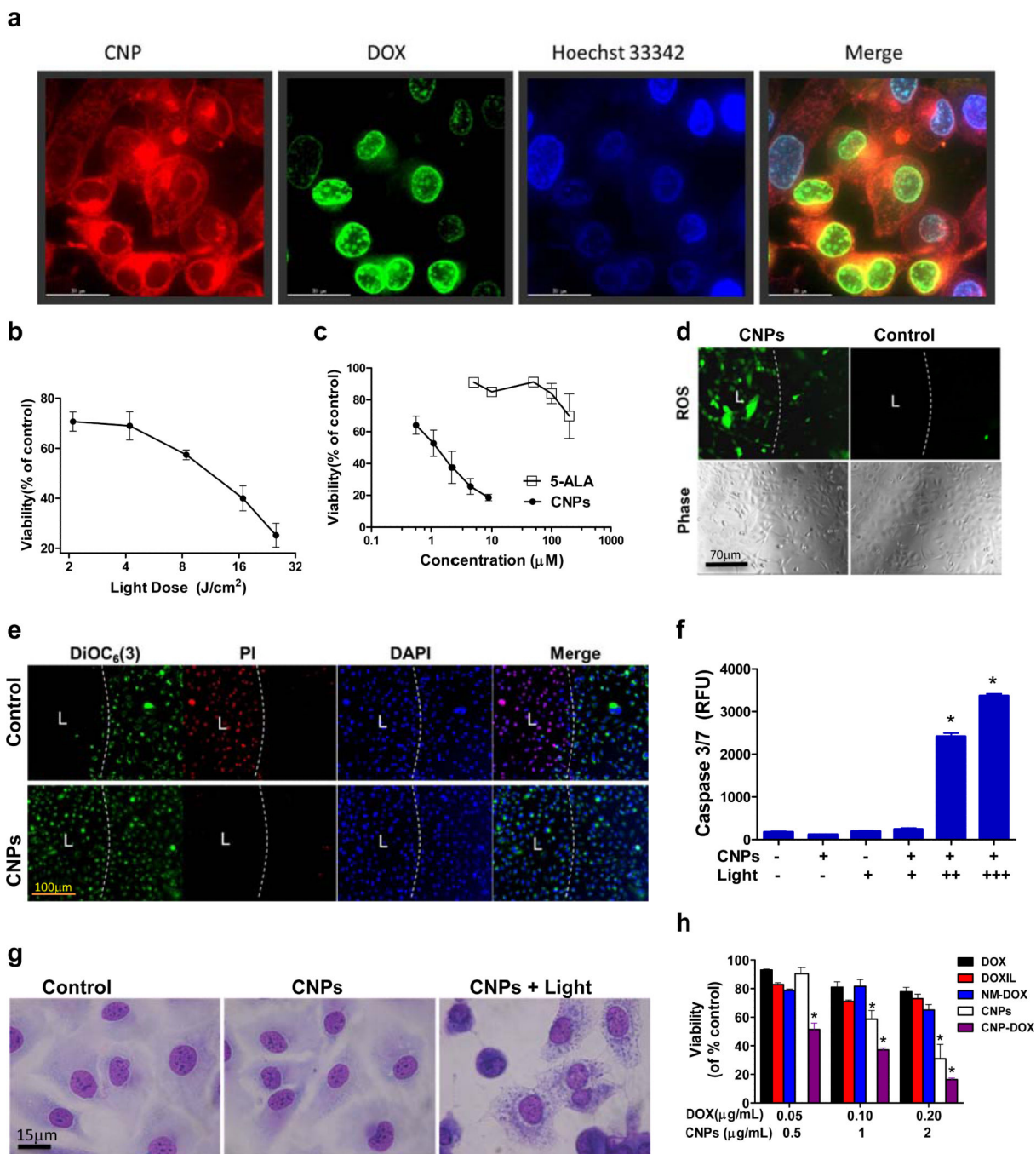
Figure 3. Intracellular delivery and photo-cytotoxicity of nanoporphyrins against cancer cells
(**a**) Uptake of DOX (**green**) loaded CNPs (**red**) in SKOV3 ovarian cancer cell line. Cells were cultured in the 8 well chamber cover glass slides overnight. Cells were pre-treated with Hoechst 33342 (**blue**) for 10 minutes for nucleus staining followed by incubation with CNP-DOX (DOX: 0.1mg/ml) in PBS. Imaging was acquired at 2 hrs using Deltavision deconvolution microscope. (Scale bar = 30 μm). The viability of SKOV3 ovarian cancer cells after (**b**) 2 hrs exposure to 4.4μM CNPs followed by illumination with various levels of NIR light, and (**c**) incubation with CNPs or 5-ALA for 24 hrs followed by exposure to NIR

light at 0.07 W cm^{-2} for 60 seconds. ROS mediated cell death after CNPs and light treatment of SKOV3 ovarian cancer cells: (**d**) Cells were treated with or without 2.2 μM CNPs for 24 hrs and loaded with DCF-DA for 30 min. After treatment with NIR light at 0.07 W cm^{-2} for 60 seconds, images were acquired by fluorescence microscopy to detect ROS production; (**e**) SKOV3 ovarian cancer cells were incubated with 2.2 μM CNPs for 24 hrs in 96-well black-wall plate, stained with 40 nM of DiOC$_6$(3) (Green, Ψm^{high}) for 20 min at the end of incubation to evaluate mitochondria membrane potential(Ψm), and followed by illumination of a portion of each well to elicit PDT effect. The illumination area was marked with "L". 24 hrs later, the cells were stained with propridium iodide (PI) for cell death. (**f**) Cells were treated with different concentrations of CNPs for 24 hrs followed by PDT. 24 hrs later, caspase3/7 activity was measured by SensoLyte® kit (Anaspec, Fremont, CA). (**g**) Cell morphology after PDT. SKOV3 ovarian cancer cells were cultured on 8-well chamber slides and treated for 24 hrs with PBS, CNPs alone and combination of CNPs and light (at 0.07 W cm^{-2} for 60 seconds). Cells were then fixed and stained with Hema3® after 2 hrs. Cells treated with CNPs+light exhibited obvious nucleus swelling, cell rounding, membrane damage, and cytoplasm aggregation. (**h**) Cytotoxicity effect from combination of doxorubicin with CNPs mediated photo-therapy: SKOV3 ovarian cancer cells were treated with CNPs alone, doxorubicin loaded crosslinked nanoporphyrins (CNP-DOX) or doxorubicin loaded standard micelles (NM-DOX)[11] with various concentrations of DOX and/or CNPs for 24 hrs. After washing, cells were exposed with light and cell viability was measured after 24 hrs. * p<0.05, one-way ANOVA.
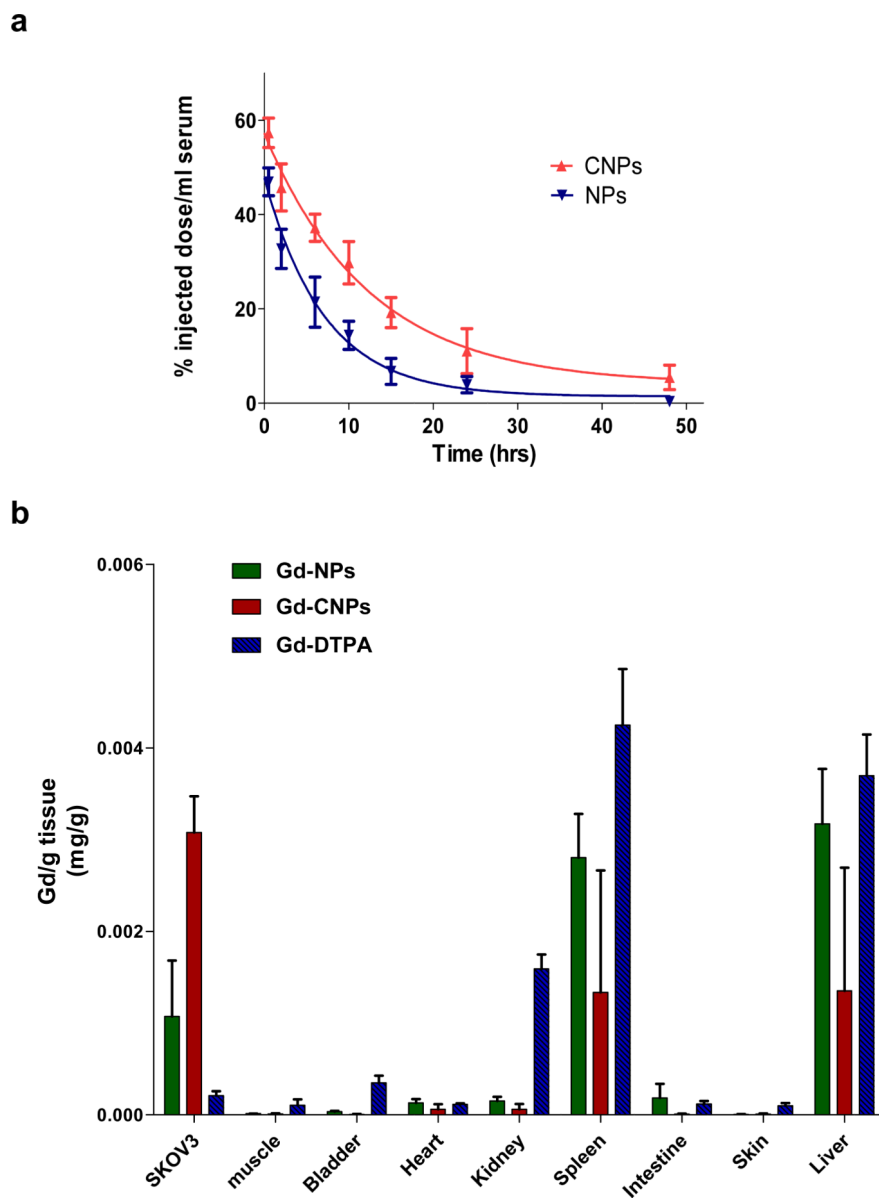
a

b

Figure 4. *In vivo* **blood elimination kinetics and biodistributions**

(a) *In vivo* blood elimination kinetics of NPs and CNPs at a dose of 5mg/kg body weight (n=3 for each group). **(b)** Gd distribution in tissues of SKOV3 ovarian cancer mice 24 hrs post-injection of Gd-DTPA, Gd-NP and Gd-CNPs, measured by inductively coupled plasma mass spectrometry (ICP-MS, Agilent Techologies, 7500ce). Three mice were used in each experiment. Mice received Gd-DTPA, Gd-NP, and Gd-CNP at the dose of Gd 20 mg/kg. After 24 hrs, mice were sacrificed. Tumor and major orangs were collected and weighted. Tissue samples were treated with 200 μl of nitric acid under 60°C for 2 hrs till most tissues were digested. Fat was digested by adding another 200 μl of 50% H_2O_2 for 2-4 hrs and total volume was adjusted to 1 ml. Equal amounts of clear samples were used for ICP-MS analysis to detect Gd concentration. Results were normalized to original tissue weight and present as mg Gd per gram tissue (n=3 for each group).
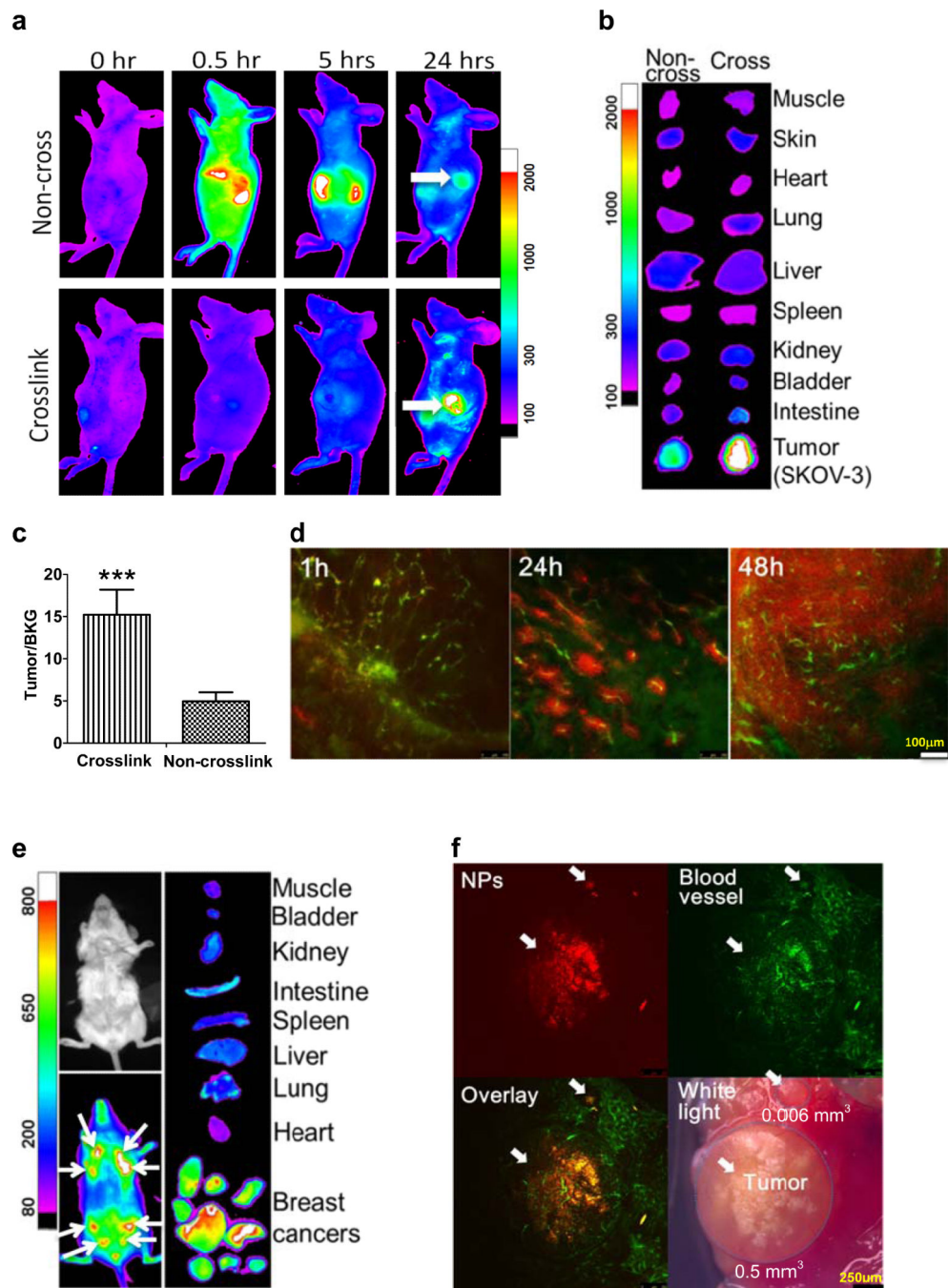
Figure 5. Nanoporphyrin mediated NIRF imaging in animal models
(**a**) Representative *in vivo* NIRF imaging of nude mice bearing SKOV3 ovarian cancer xenograft following intravenous injection of NPs and CNPs (NP dose: 25 mg/kg). The white arrow points to the tumor site. (**b**) Representative *ex vivo* NIRF imaging of SKOV3 ovarian cancer xenograft 24 hrs post-injection of NPs (left) and CNPs (right). (**c**) Quantitative NIRF fluorescence in tumor SKOV3 at 24 hrs post-injection of NPs and CNPs ((n=4) (NP dose: 25 mg/kg). Images were analyzed as the average signal in the region of interest (ROI) in tumor and normalized to muscle. *** p<0.001, *t*-test. (**d**) Projection images of the

distribution of CNPs in SKOV3 tumor at 1, 24, 48 hrs post injection observed by Large-Scale-Imaging (LSI) laser scanning confocal microscope. Red: CNPs; Green: Dextran-FITC labelled tumor blood vessel.. **(e)** The representative *in vivo* and *ex vivo* NIRF light imaging of transgenic mice with mammary cancer (FVB/n Tg(MMTV-PyVmT) at 24 hrs post-injection of CNPs (NP dose: 25 mg/kg). The white arrows point to the tumor site. Tumor volume was calculated by $(L*W^2)/2$, where L is the longest, and W is the shortest tumor diameter (mm). **(f)** The accumulation of CNPs in lung metastasis of breast cancer in transgenic mice at 24 hrs post injection observed by LSI laser scanning confocal microscope. The white arrow points to the metastatic site. Red: nanoporphyrins; Green: Dextran-FITC labelled tumor blood vessel.
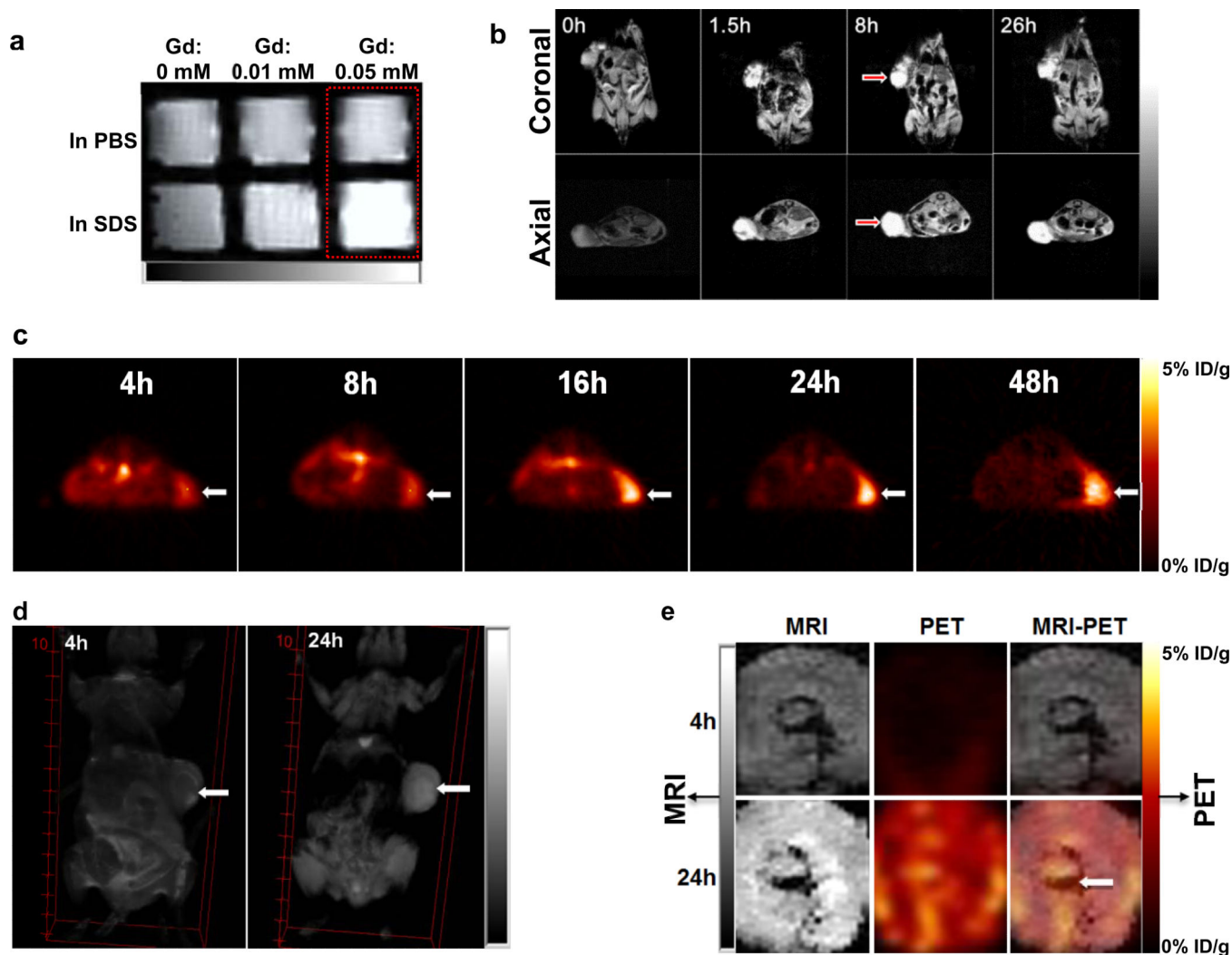
Figure 6. Nanoporphyrin mediated MRI and PET imaging in animal models
(a) *In vitro* MRI signal of Gd-NPs in the absence and in the presence of SDS obtained by T1-weighted MR imaging on a Bruker Biospec 7T MRI scanner using a FLASH sequence.
(b) Representative coronal and axial MR images of transgenic mice with mammary cancer (FVB/n Tg(MMTV-PyVmT) using a FLASH sequence pre-injection and after injection of 0.15 mL Gd-NPs (Gd dose: 0.015 mmole/kg). The white arrow points to the tumor site. (c) PET image of nude mice bearing SKOV3 ovarian cancer xenografts at 4, 8, 16, 24, 48 hrs post-injection of ^{64}Cu-labeled NPs (150-200 μL, ^{64}Cu dose: 0.6-0.8 mCi). The white arrow points to the tumor site. (d) 3D coronal MR images of nude mice bearing A549 lung cancer xenografts using a FLASH sequence at 4 or 24 hrs post-injection with 0.15 mL of ^{64}Cu and Gd dual-labeled NPs (150-200 μL, ^{64}Cu dose: 0.6-0.8 mCi, Gd dose: 0.015 mmole/kg). The white arrow points to the tumor site. (e) PET-MR images of tumor slices of nude mice bearing A549 lung cancer xenograft at 4 or 24 hrs post injection of dual-labeled NPs. White arrow points to the necrotic area in the center of the tumor.
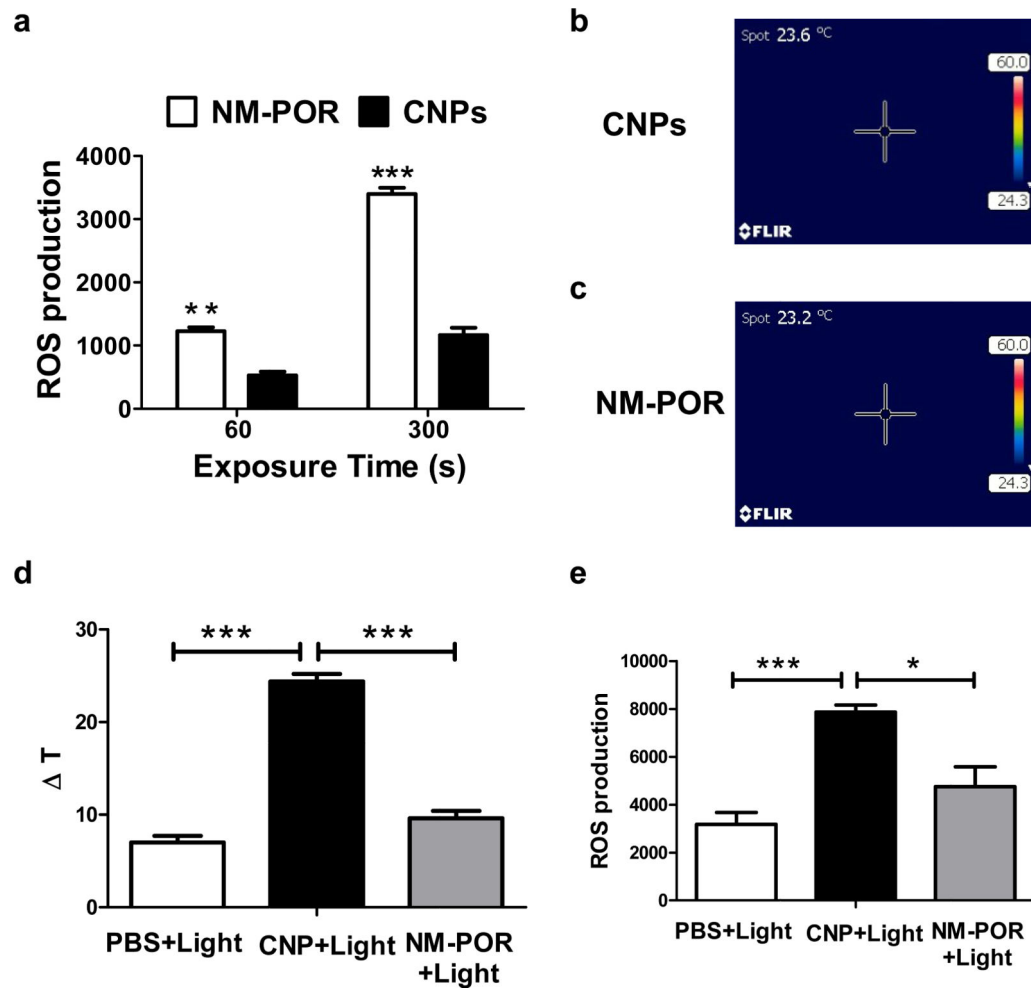
Figure 7. ROS production and heat generation in blood and at tumor tissue
(a) ROS production of blood drops drawn from nude mice bearing implanted tumor xenografts 1 min post-injection of CNPs and NM-POR (Por dose: 5 mg/kg) after light exposure, and was measured by DCF-DA as ROS indicator. Light dose: 0.1 W for 60 s and 300 s. **p< 0.002, ***p< 0.001, *t*-test. The temperature of blood drops drawn from nude mice bearing implanted tumor xenografts 1 min post-injection of **(b)** CNPs and **(c)** NM-POR (Por dose: 5 mg/kg) after light exposure. Light dose: 0.1 W for 300 seconds. The temperature was monitored by a FLIR thermal camera. **(d)** The temperature changes (T) at tumors of nude mice bearing implanted SKOV3 tumor xenografts 24 hrs post-injection of PBS, CNPs, and NM-POR (Por dose: 5 mg/kg) after light exposure (n=5). Light dose: 1.25 W/cm^2 for 120 seconds. The temperature was monitored by a FLIR thermal camera. ***p< 0.001, one-way ANOVA. **(e)** ROS production at tumors of nude mice bearing implanted tumor xenografts 24 hrs post-injection of PBS, CNPs and NM-POR (Por dose: 5 mg/kg) after light exposure (n=5). Light dose: 1.25 W/cm^2 for 120 seconds. Measured by using DCF-DA as a ROS indicator. *p< 0.01, ***p< 0.001, one-way ANOVA.
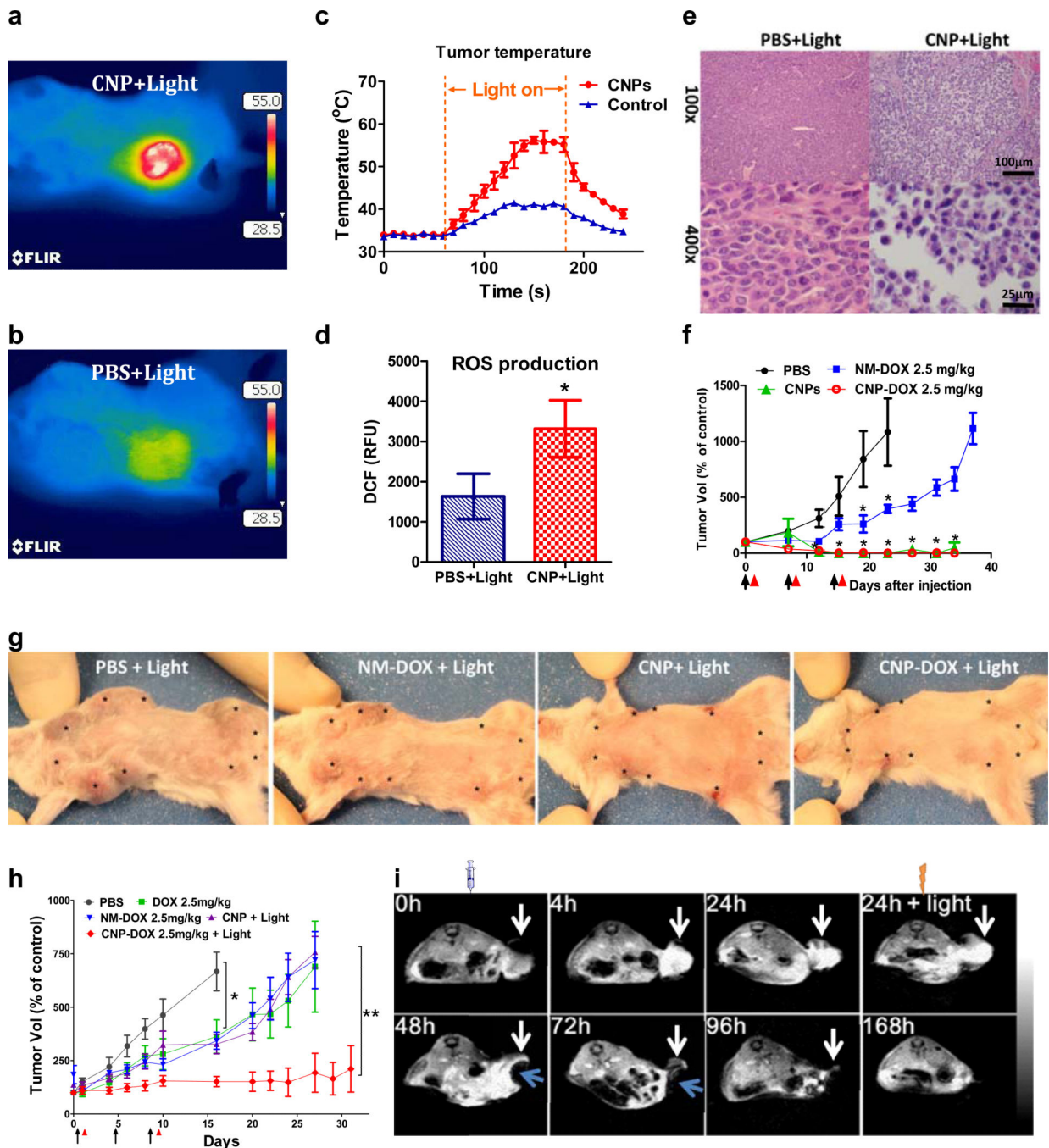
Figure 8. Nanoporphyrin mediated multimodal therapy in animal models and imaging-guided delivery

Representative thermal images of tumors in transgenic mice with mammary cancer (FVB/n Tg(MMTV-PyVmT) after light irradiation at 24 hrs post-injection of (**a**) CNPs and (**b**) PBS. (**c**) Temperature change in tumors in transgenic mice injected with CNPs and PBS before and after irradiation. (**d**) ROS production at tumor site in transgenic mice treated with CNPs and PBS (control) for 24 hrs followed by laser irradiation by using DCF-DA as an indicator. p<0.025, t-test. (**e**) Histopathology of tumors from mice injected with PBS or CNPs 24 hrs

after irradiation. The light dose was 1.25 W cm^{-2} for 2 min while the NPs dose was 25 mg/kg (equivalent to 5 mg/kg of Por) for **a-e**. **(f)** Tumor volume change of transgenic mice with mammary cancer (n=8) treated with CNPs, CNP-DOX and NM-DOX (standard micelles without porphyrin)[21] on day 0, 7, and 14 (black arrow) followed by light exposure on the tumors in the mice in all groups at 24 hrs post-injection (red arrow). p< 0.01, one-way ANOVA. DOX dose: 2.5 mg/kg, NP dose: 25 mg/kg (equivalent to 5 mg/kg of Por), light dose: 1.25 W cm^{-2} for 2 min. **(g)** Pictures of transgenic mice at day 34 of the treatment. (*****: mammary tumors) **(h)** Tumor volume change of mice (n=8) bearing SKOV3 ovarian cancer xenograft treated with CNPs and CNP-DOX at day 0, 4 and 8 (black arrow) followed by irradiation on day 1, and 9 (red arrow). PBS and NM-DOX were injected for comparison. DOX dose: 2.5 mg/kg, NP dose: 25 mg/kg (equivalent to 5 mg/kg of Por), light dose: 0.25 W cm^{-2} for 2 min. p< 0.01, one-way ANOVA. **(i)** MRI guided PTT/PDT: representative MR images of mice injected with Gd-NPs (Gd dose: 0.015 mmole/kg) before and after laser irradiation. White arrows indicate the tumor sites. Images were collected at 0 (pre-injection), 4, 24, 48, 72, 96 and 168 hrs post-injection. MR imaging showed large signal voids (blue arrows) at tumor sites 24 hrs after irradiation (48 hrs post-injection) at a dose of 1.25 W cm^{-2} for 3 min and the tumors were completely ablated at 168 hrs (7 days) post-injection.